Journal of
Nanoelectronics and Optoelectronics
Vol. 1, 19–38, 2006

ZnO Quantum Dots: Physical Properties and Optoelectronic Applications

Vladimir A. Fonoberov and Alexander A. Balandin*

Nano-Device Laboratory, University of California–Riverside, Riverside, California 92521, USA

(Received 28 January 2006; accepted 01 March 2006)

We present a review of the recent theoretical and experimental investigation of excitonic and phonon states in ZnO quantum dots. A small dielectric constant in ZnO leads to very large exciton binding energies, while wurtzite crystal structure results in unique phonon spectra different from those in cubic crystals. The exciton energies and radiative lifetimes are determined in the intermediate quantum confinement regime, which is pertinent to a variety of realistic ZnO quantum dots produced by wet chemistry methods. An analytical model for the interface and confined polar optical phonons is presented for spheroidal quantum dots of different size and barrier materials. The experimental part of the review covers results of the nonresonant and resonant Raman spectroscopy and photoluminescence study of ZnO quantum dots with sizes comparable to or larger than the exciton diameter in ZnO. The origins of the Raman phonon shifts and the mechanisms of the carrier recombination in ZnO quantum dots are discussed in detail. The reviewed properties of ZnO quantum dots are important for the proposed optoelectronic applications of these nanostructures.

CONTENTS

1. INTRODUCTION

Nanostructures and heterostructures made of zinc oxide (ZnO) have already been used as transparent conductors in solar cells, as components in high-power electronics, UV light emitters, and gas and chemical sensors. Recently, ZnO nanostructures attracted attention for possible applications in optoelectronic and spintronic devices, such as light-emitting and laser diodes with polarized output, spin-based memory, and logic. In this review, we describe physical properties of a specific type of ZnO nanostructure: quantum dots (QDs). We focus our discussion on the excitonic and phonon processes in ZnO QDs and their effect on optical response of these nanostructures. The review contains both theoretical and experimental results pertinent to ZnO QDs and their optoelectronic applications.

Compared to other materials with a wide band gap, ZnO has a very large exciton binding energy (~ 60 meV), which results in more efficient excitonic emission at room temperature. Moreover, it is believed that exchange interaction between spins of *acceptor*-bound charge carriers can mediate room temperature ferromagnetic ordering in ZnO. Since doping of semiconductor QDs is a rather challenging task,[1] the existence of various unintentional "useful" impurities in ZnO nanostructures may be advantageous for optoelectronic and spintronic applications. Well-established colloidal fabrication techniques give ZnO QDs of nearly spherical shape with diameters less than 10 nm. Thus, various properties of colloidal ZnO QDs, such as exciton energy and radiative lifetime, are expected to be strongly affected by quantum confinement. Wurtzite crystal structure and the spherical shape of ZnO QDs are also expected to result in strong modification of optical phonon (lattice vibration) modes in comparison with bulk ZnO phonons.

*Author to whom correspondence should be addressed. E-mail: balandin@ee.ucr.edu

Vladimir A. Fonoberov received his M.S. degree in Physics (1999) and Ph.D. degree in Physical and Mathematical Sciences (2002) from the Moldova State University. Since 2003 he has been working as a Postdoctoral Researcher in the Electrical Engineering Department of the University of California, Riverside. Dr. Fonoberov's research interests are in the area of theoretical nanoscience and nanotechnology. His current research topics include optical and spintronic properties of ZnO nanostructures. He contributed to theoretical investigation of optoelectronic properties of quantum-dot heterostructures and electronic transport in hybrid nanowires. He has authored more than 20 journal publications and a book chapter. Research work of Dr. Fonoberov was recognized by the NSF-NATO Award in Science and Engineering (2003). He is a member of the American Physical Society.

Alexander A. Balandin received his M.S. degree in Applied Physics and Mathematics from the Moscow Institute of Physics and Technology, Russia in 1991. He received his Ph.D. degree in Electrical Engineering from the University of Notre Dame, USA, in 1996. He worked as a Research Engineer in the Electrical Engineering Department of the University of California, Los Angeles, USA, from 1997 to 1999. In July 1999, he joined the Department of Electrical Engineering at the University of California, Riverside, USA, where he is a Professor. He leads the Nano-Device Laboratory, which he organized in 2001. In 2005 he was a Visiting Professor at Cambridge University, UK. Professor Balandin's research interests are in the area of electronic materials, nanostructures, and nanodevices. Current research topics in his group include phonon engineering at nanoscale, electron and thermal transport in nanostructures, wide band-gap semiconductors and devices, hybrid bioinorganic nanosystems, and electronic noise phenomena. He contributed to investigation of noise in high-power GaN-based field-effect transistors, excitonic processes, and phonon transport in semiconductor nanostructures. He has authored more than 80 journal publications and 10 invited book chapters. He edited the books *Noise and Fluctuations Control in Electronic Devices* (2002) and *Handbook of Semiconductor Nanostructures and Nanodevices* (2006). He chaired the SPIE International Conference on Noise in Electronic Devices and Circuits (2005) and several international conference sessions. He is Editor-in-Chief of the *Journal of Nanoelectronics and Optoelectronics* and serves on the editorial board of the *Journal of Nanoscience and Nanotechnology*. His research work was recognized by the ONR Young Investigator Award (2002), National Science Foundation CAREER Award (2001), University of California Regents Award (2000), and the Merrill Lynch Innovation Award for "commercially valuable engineering research" (1998). He is a Senior Member of IEEE, a member of APS, AAAS, Electrochemical Society, SPIE, and Eta Kappa Nu. More information on his research can be found at http://ndl.ee.ucr.edu/

2. EXCITONIC PROPERTIES OF ZINC OXIDE QUANTUM DOTS

Interpretation of experimental data and optimization of ZnO QDs for optoelectronic device applications require a theoretical model for prediction of the energy and the oscillator strength of optical transitions. Due to specifics of the wurtzite ZnO material system, such as degeneracy and anisotropy of the valence band as well as small dielectric constant and correspondingly strong electron-hole Coulomb interaction, simple one-band effective-mass models fail to give correct results. Recently, the tight-binding method has been used to compute the electron and hole states in ZnO QDs.[2] The electron-hole interaction in Ref. 2 was taken into account by adding the exciton binding energy of $-1.8\,e^2/\varepsilon R$ (Ref. 3) to the energy of an electron-hole pair. However, Brus[4] has shown that the treatment of an exciton in ZnO QDs as an electron-hole pair is a rather poor approximation, leading to significant errors. The pseudopotential model, which was shown to describe exciton states in a CdSe QD[5] very well, to the best of our knowledge has not been applied to ZnO QDs.

In this section, we focus on the properties of the lowest excitonic states in colloidal, nearly spherical ZnO QDs with diameters in the range from 2 to 6 nm. Fonoberov et al.[6] demonstrated that the multiband effective mass model works surprisingly well for the description of lowest exciton states even for quantum shells[7] as thin as one monolayer. Here, we employ this model, with some modifications,[8] to calculate the lowest exciton states in ZnO QDs. In our numerical computations, we have employed the following effective mass parameters of wurtzite ZnO[9]: electron effective mass $m_e = 0.24$; Rashba-Sheka-Pikus parameters of the valence band $A_1 = -3.78$, $A_2 = -0.44$, $A_3 = 3.45$, $A_4 = -1.63$, $A_5 = -1.68$, $A_6 = -2.23$, $A_7 = 0.47\ \text{nm}^{-1}$; crystal-field splitting energy $\Delta_{cr} = 38$ meV; and optical dielectric constant $\varepsilon = 3.7$. The band gap energy of wurtzite ZnO is $E_g = 3.437$ eV[10]. The heavy-hole effective mass can be estimated as $m_{hh} \approx 1/|A_2| = 2.27$, which gives the ratio $m_{hh}/m_e = 9.5$, in agreement with the tight-binding calculations.[11] Using the reduced exciton mass $\mu = m_e m_{hh}/(m_e + m_{hh})$, the exciton Bohr radius is estimated to be $a_B = 4\pi\varepsilon_0\hbar^2\varepsilon/e^2 m_0\mu = 0.90$ nm.

Since the exciton Bohr radius a_B in bulk ZnO is about 0.9 nm, the size of the considered QDs is two to three times larger than the size of the bulk exciton. This results in comparability of the strength of the electron-hole Coulomb interaction and quantum confinement effects. Therefore, one cannot use either the "strong confinement" or "weak confinement" approximations[12] to obtain exciton states in such ZnO QDs. The strong confinement approximation ($R/a_B < \sim 2$) assumes that the electron and hole confinement energies are much larger than the Coulomb interaction energy, and the electron and hole wave

functions can be treated separately. The weak confinement limit ($R/a_B > \sim 4$) uses the assumption that Coulomb interaction is strong compared to quantum confinement, and as a result, the exciton wave function can be decomposed into the wave function of the exciton center of mass and the wave function of the relative electron-hole motion.

To determine excitonic states in ZnO QDs in the intermediate confinement regime, which is relevant to the reported experimental data and important for possible device applications, we solve the six-dimensional exciton problem. In the case of isotropic nondegenerate conduction and valence bands, the six-dimensional problem for spherical QDs can be reduced to a three-dimensional one with independent variables r_e, r_h, and θ', where θ' is the angle between the electron radius-vector $\mathbf{r}_e$ and hole radius-vector $\mathbf{r}_h$. However, the valence band of ZnO is degenerate and anisotropic. Therefore, we can only reduce the exciton problem to a five-dimensional one by making use of the axial symmetry of exciton wave functions along the c-axis of wurtzite ZnO. We calculate the exciton states using the following Hamiltonian:

$$\hat{H}_{exc} = [\hat{H}_e + V_{s-a}(\mathbf{r}_e)] - [\hat{H}_h - V_{s-a}(\mathbf{r}_h)] + V_{int}(\mathbf{r}_e, \mathbf{r}_h), \quad (1)$$

where the two-band electron and the six-band hole Hamiltonians $\hat{H}_e$ and $\hat{H}_h$ for wurtzite nanocrystals have been written explicitly in Ref. 13. Since dielectric constants in ZnO QDs and the exterior medium are different, the Coulomb potential energy of the electron-hole system in Eq. (1) is represented by the sum of the electron-hole interaction energy $V_{int}(\mathbf{r}_e,\mathbf{r}_h)$ and electron and hole self-interaction energies $V_{s-a}(\mathbf{r}_e)$ and $V_{s-a}(\mathbf{r}_h)$ defined in Refs. 4 and 14. Neglecting a very small spin-orbit splitting, which is about 10 meV[9, 10] for ZnO, we can simplify the exciton problem by using the one-band electron and the three-band hole Hamiltonians.

We choose the coordinate system in such a way that the z-axis is parallel to the c-axis of wurtzite ZnO. Due to the axial symmetry of the exciton problem, the z-component of the exciton angular momentum M_z is a good quantum number. To compute the eigenstates of the Hamiltonian (1), we represent the three-component exciton envelope function in the form

$$\Psi_{M_z}(\mathbf{r}_e, \mathbf{r}_h) = \frac{1}{2\pi} \sum_{m=-\infty}^{\infty} \begin{pmatrix} \Psi_{-1}^{M_z,m}(\rho_e, z_e; \rho_h, z_h)\, e^{i(m-1)\varphi} \times e^{i(M_z-1)\Phi} \\ \Psi_{0}^{M_z,m}(\rho_e, z_e; \rho_h, z_h)\, e^{im\varphi} \times e^{iM_z\Phi} \\ \Psi_{1}^{M_z,m}(\rho_e, z_e; \rho_h, z_h)\, e^{i(m+1)\varphi} \times e^{i(M_z+1)\Phi} \end{pmatrix}, \quad (2)$$

where Ψ_{-1}, Ψ_0, and Ψ_1 are the components of exciton envelope function in front of the Bloch functions $\left|S\frac{X+iY}{\sqrt{2}}\right\rangle$, $|SZ\rangle$, and $\left|S\frac{X-iY}{\sqrt{2}}\right\rangle$, respectively. In Eq. (2), the angles φ and Φ describe the relative angular motion of the electron and the hole and their angular motion as a whole, correspondingly. Substitution of the wave function (2) into the envelope-function equation with Hamiltonian (1) gives the system of three five-dimensional differential equations with respect to functions $\Psi_{\alpha}^{M_z,m}(\rho_e, z_e;\rho_h, z_h)$. The obtained system is solved numerically using the finite difference method. In the numerical calculation, we have neglected the small penetration of the exciton wave function into the exterior medium.

To validate the model, we calculated exciton ground-state energy as a function of the QD radius for spherical ZnO QDs in water and compared it with experimental data reported in Refs. 15 and 16. As one can see in Figure 1, our theoretical results are in excellent agreement with measurements. We have studied the influence of the QD shape and the exterior medium on the exciton ground-state energy. Transmission electron microscopy (TEM) images of ZnO QDs show that a fraction of QDs are not spherical but rather prolate ellipsoids with about a 9/8 ratio of semiaxes.[16] Our calculations show that prolate ZnO QDs have smaller exciton ground-state energy than spherical QDs with the same semiminor axis (shown by the dashed line in Fig. 1). If we consider ZnO QDs in air ($\varepsilon = 1$) instead of water ($\varepsilon = 1.78$), the exciton ground-state energy increases (shown by the dotted line in Fig. 1). The difference in the ground-state energies due to the change of the ambient (water → air) decreases from 70 to 13 meV when the QD radius increases from 1 to 3 nm. Overall, it is seen from our calculations that small size dispersion of ZnO QDs and different exterior media have relatively small influence on the exciton ground-state energy for the QDs with radius above 1.5 nm.

Interpretation of experimental data as well as prediction of the optical properties for ZnO QDs require the

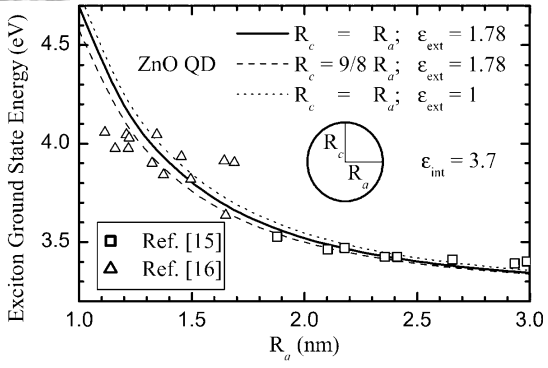

Fig. 1. Calculated exciton ground-state energy in ZnO QDs as a function of the QD radius (semiaxis) for spherical (ellipsoidal) QDs. Results are shown for two different ambient media: water ($\varepsilon = 1.78$) and air ($\varepsilon = 1$). For comparison, we show experimental data points from Refs. 15 and 16. Reprinted with permission from Ref. 8, V. A. Fonoberov and A. A. Balandin, *Phys. Rev. B*, 70, 195410 (**2004**). © 2004, American Physical Society.

knowledge of transition energies and their oscillator strength. The size dependence of the excited exciton states in spherical ZnO QDs is shown in Figure 2. The energy of the excited states is counted from the exciton ground-state energy. Figure 2 shows the size dependence of a few lowest exciton states with $|M_z| = 0, 1, 2$. The oscillator strength f of an exciton state with energy E_{exc} and envelope wave function $\Psi_{\text{exc}}(\mathbf{r}_e, \mathbf{r}_h)$ is calculated as[13]

$$f = \frac{E_P}{E_{\text{exc}}} \left| \int_V \Psi_{\text{exc}}^{(\alpha)}(\mathbf{r}, \mathbf{r}) d\mathbf{r} \right|^2 \tag{3}$$

where the Kane energy of ZnO is $E_P = 28.2$ eV.[17] In Eq. (3), α denotes the component of the wave function active for a given polarization. In the dipole approximation, only exciton energy levels with $|M_z| = 0, 1$ can be optically active; that is, they can have a nonzero oscillator strength. Besides, the exciton energy levels with $M_z = 0$ ($M_z = \pm 1$) are optically active only for the polarization $\mathbf{e} \parallel \mathbf{z}$ ($\mathbf{e} \perp \mathbf{z}$). The oscillator strengths of the corresponding exciton energy levels are depicted in Figure 2 with circles. The size of the circles is proportional to the oscillator strength. We can see that there are two exciton levels that have large oscillator strengths. They are the first level with $|M_z| = 1$, which is the exciton ground state, and the second level with $M_z = 0$. The energy difference between the two exciton levels decreases while their oscillator strengths, which are almost the same for both levels, increase with the increasing the QD size. Other exciton energy levels shown in Figure 2 have zero or negligible oscillator strength.

Figure 3 shows the optically active component of the exciton wave function (with equal electron and hole coordinates) for each of the two brightest exciton states from Figure 2 for QD radii 1, 2, and 3 nm. For QDs with $R > a_B$, the electron and hole motion around their center of mass prevents the center of mass from reaching the QD surface, thus forming a so-called dead layer near the QD surface.

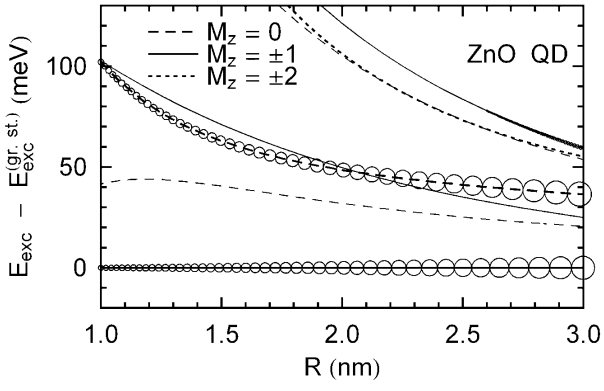

Fig. 2. Energies of the excited exciton states (counted from the exciton ground state) as a function of the radius of spherical ZnO QDs in water. The oscillator strength of the corresponding transitions is depicted with circles. The size of the circles is proportional to the oscillator strength.

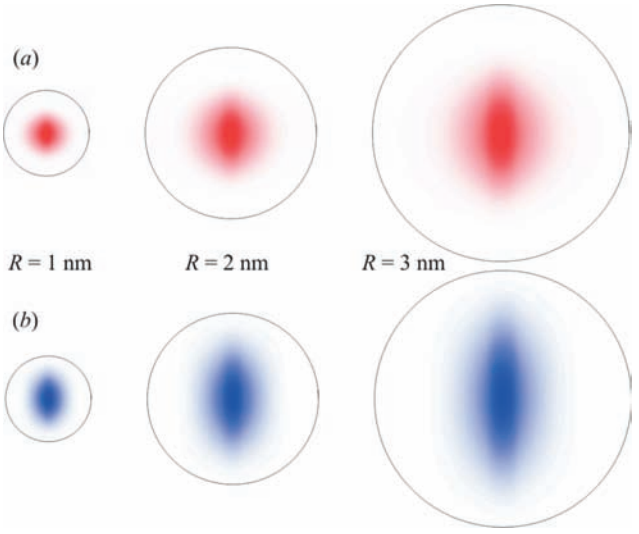

Fig. 3. Optically active component of the exciton wave function (with equal electron and hole coordinates) of the first (a) and the second (b) bright exciton states for three different sizes of spherical ZnO QDs in water. The c-axis of wurtzite ZnO is directed vertically.

The concept of the exciton dead layer can be traced back to Pekar.[18] It states that the exciton is totally reflected from an effective barrier located inside the QD at the distance d from the QD surface. To estimate the thickness d of the dead layer in ZnO QDs, we assume that only the optically active component of the exciton wave function is nonzero, which allows us to approximate the wave function of the exciton center of mass as

$$\Psi_{\text{exc}}(\mathbf{r}, \mathbf{r}) = \frac{1}{\sqrt{\pi a_B^3}} \frac{\sin(\pi r/(R-d))}{r\sqrt{2\pi(R-d)}}. \tag{4}$$

Assuming that Eq. (4) correctly reproduces the density of the exciton's center of mass, we can find the thickness d of the dead layer and the exciton Bohr radius a_B from the following system:

$$\begin{cases} \sqrt{\dfrac{8(R-d)^3}{\pi^2 a_B^3}} = \displaystyle\int_V \Psi_{\text{exc}}^{(\alpha)}(\mathbf{r}, \mathbf{r})\, d\mathbf{r}, \\ \dfrac{1}{\sqrt{2a_B^3(R-d)^3}} = \Psi_{\text{exc}}^{(\alpha)}(0, 0). \end{cases} \tag{5}$$

Note that the system of Eq. (5) is an identity when the optically active component $\Psi_{\text{exc}}^{(\alpha)}(\mathbf{r}, \mathbf{r})$ of the wave function of exciton ground state is given by Eq. (4). The fitting parameters d and a_B found as solutions of system (5) are plotted in Figure 4 as a function of the radius of ZnO QD in water. The quality of the fit is illustrated in Figure 5 for the ZnO/water QD with $R = 2$ nm. It is seen from Figure 4 that the dead-layer thickness d increases almost linearly with R, while the exciton Bohr radius tends to its bulk

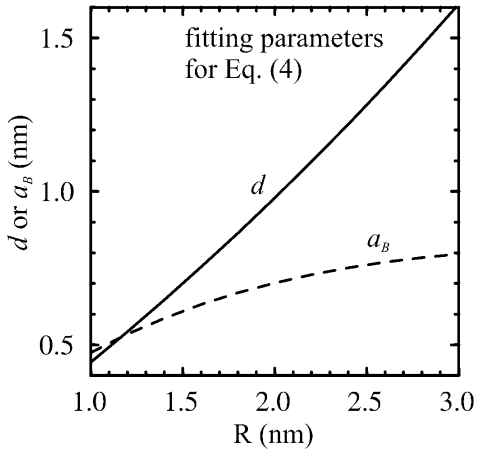

Fig. 4. Fitting parameters for Eq. (4) as a function of ZnO QD radius; d is the dead layer thickness, and a_B is the exciton Bohr radius.

value (0.9 nm). Figure 3 confirms that the thickness of the dead layer increases with increasing the QD size. Our estimate gives the value of the dead-layer thickness $d = 1.6$ nm for $R = 3$ nm, which almost coincides with the dead-layer thickness calculated in Ref. 19 for a quantum well with thickness $L \gg a_B$ and $m_{hh}/m_e = 9.5$. The latter suggests that the thickness of the dead layer for larger ZnO QDs (i.e., in the weak confinement regime) is not noticeably larger than 1.6 nm. The relatively large thickness of the dead layer in colloidal ZnO QDs is attributed to the large ratio of hole and electron effective masses.

The fact that the exciton in the spherical ZnO QDs is prolate along the c-axis (see Fig. 3) is attributed to the anisotropy of the valence band of wurtzite ZnO. It is also seen from Figure 3 that the exciton is more prolate for the second optically active state than it is for the first one. The exciton center of mass is prolate along the c-axis of wurtzite ZnO and squeezed to the center of the ZnO QD.

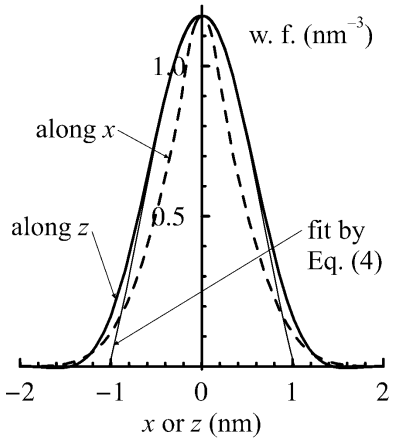

Fig. 5. Wave function of the exciton's center of mass along x- and z-axes for the 4-nm diameter ZnO QDs; thin solid line shows a fit by Eq. (4).

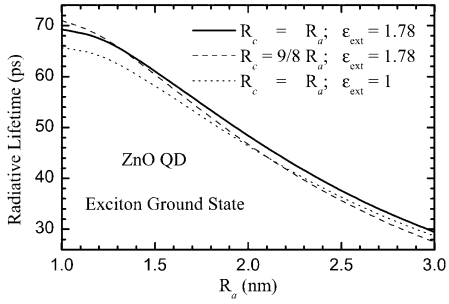

Fig. 6. Radiative lifetime of the exciton ground state in ZnO QDs as a function of the QD radius (semiaxis) for spherical (ellipsoidal) QDs. Reprinted with permission from Ref. 8, V. A. Fonoberov and A. A. Balandin, *Phys. Rev. B*, 70, 195410 (**2004**). © 2004, American Physical Society.

The above behavior of the exciton in a colloidal ZnO QD should strongly affect the exciton radiative lifetime.

The radiative recombination lifetime τ of excitons in bulk ZnO is about 322 ps,[20] which is small compared to other semiconductors. It is well known that the oscillator strength of localized excitons is substantially higher than that of free excitons.[21] Since the excitons are confined in ZnO QDs and the radiative lifetime is inversely proportional to the oscillator strength

$$\tau = \frac{2\pi\varepsilon_0 m_0 c^3 \hbar^2}{n e^2 E_{exc}^2 f}, \tag{6}$$

one can expect for ZnO QDs very small exciton radiative lifetimes, on the order of tens of picoseconds. In Eq. (6), ε_0, m_0, c, $\hbar$, and e are fundamental physical constants with their usual meaning, and n is the refractive index. To the best of our knowledge, no measurements of the exciton lifetime in ZnO QDs have been carried out. However, it has been established that the exciton lifetime is less than 50 ps for ZnO QDs with diameter 5 nm.[22]

The calculated radiative lifetime of the excitons in the ground state is shown in Figure 6 as a function of the QD size. The solid line in Figure 6 represents the radiative lifetime in the spherical ZnO QD in water, the dashed line shows the lifetime in the prolate ZnO QD in water, and the dotted line gives the lifetime in the spherical ZnO QD in air. For the QD with diameter 5 nm, we obtain a lifetime of about 38 ps, in agreement with the conclusion in Ref. 22. We can see that the influence of the QD ellipticity and the exterior medium on the radiative lifetime in ZnO QDs is relatively weak. Analyzing the calculated dependence of the exciton lifetime on the radius of the spherical ZnO QD in water, we found that it can be fitted accurately with the function $\tau_o/[1 + (R/R_o)^3]$, where $\tau_o = 73.4$ ps and $R_o = 2.55$ nm. For larger QDs (i.e., in the weak confinement regime), the exciton lifetime is known to be inversely proportional to the QD volume. Indeed, in this case substituting Eq. (4) into Eq. (3), one estimates $f \sim (R - d)^3/a_B^3$ and, therefore, $\tau \sim a_B^3/(R - d)^3$.

3. SURFACE IMPURITIES AND OPTICAL PROPERTIES OF ZINC OXIDE QUANTUM DOTS

Lately, there have been a number of reports of fabrication and structural and optical characterization of ZnO QDs.[15–16, 22–27] Different fabrication techniques[23, 27] and methods of the QD surface modification[24, 26] have been used to quench the defect-related green photoluminescence (PL) and enhance the UV emission from ZnO QDs. However, the nature of the UV PL from ZnO QDs itself is not fully understood. Some authors attribute the UV PL to the recombination of confined excitons, while others argue that the emission comes from surface impurities or defects. Understanding the origin of UV PL in ZnO QDs is important from both fundamental science and proposed optoelectronic applications points of view. In this section, we address this issue by examining theoretically the optical properties of ZnO QDs with ionized impurities at the QD surface. We limit our consideration to spherical QDs with diameters in the range from 2 to 6 nm.

There are only a few reports on the calculation of exciton states in the presence of charges at the QD surface.[28–30] Using the empirical pseudopotential method, Wang et al.[28, 29] studied the influence of an external charge on the electron-hole pair in the spherical CdSe QD. The electron-hole interaction in Ref. 29 was averaged so that the exciton problem was reduced to two single particle problems. While this is a good approximation for the 4-nm diameter CdSe QDs, it is not acceptable for ZnO QDs of the same size. This difference comes from the fact that the exciton Bohr radius in ZnO is only 0.9 nm. Since the size of ZnO QDs is only two to three times larger than the size of the exciton, a two-particle problem has to be solved for an exciton in ZnO QDs. The solution of a two-particle problem is a challenging task for atomistic tight-binding or pseudopotential methods. On the other hand, the multiband effective mass method works surprisingly well for the description of lowest exciton states even for quantum shells as thin as one monolayer.[6] To solve the six-dimensional exciton problem (it can be reduced to a five-dimensional one by making use of the axial symmetry of exciton wave functions along the c-axis in wurtzite ZnO), we employ the latter method adapted by us for ZnO QDs in Ref. 30.

The exciton Hamiltonian with an ionized impurity present at the QD surface is written as

$$\hat{H}_{exc} = [\hat{H}_e + V_{s-a}(\mathbf{r}_e)] - [\hat{H}_h - V_{s-a}(\mathbf{r}_h)] + V_{int}(\mathbf{r}_e, \mathbf{r}_h) + \alpha(V_{int}(\mathbf{R}, \mathbf{r}_e) - V_{int}(\mathbf{R}, \mathbf{r}_h)), \quad (7)$$

where the two-band electron and the six-band hole Hamiltonians $\hat{H}_e$ and $\hat{H}_h$ for wurtzite nanocrystals can be found in Ref. 13. In the last term of Eq. (7), $\mathbf{R}$ is the radius-vector of the impurity, and α is the charge of the impurity in units of $|e|$ ($\alpha = 1$ for a donor and $\alpha = -1$ for an acceptor). The z-axis is chosen to be parallel to the c-axis of wurtzite ZnO. Therefore, we consider an impurity located on the z-axis to keep the axial symmetry of the problem. To calculate the exciton states, we neglect the small penetration of the exciton wave function into the exterior medium and solve the Schrödinger equation with Hamiltonian (7) using the finite-difference method[14] (a cubic grid with unit length of 0.05 nm has been used, which ensured the relative error for the exciton ground-state energy <1%). The material parameters employed for ZnO have been listed in the previous section.

The calculated optical properties of ionized donor–exciton and ionized acceptor–exciton complexes in spherical ZnO QDs are presented in Figure 7. It is seen from Figure 7a that the dead layer is observed near the QD surface for the ionized donor–exciton complex. On the contrary, Figure 7b shows that the ionized acceptor–exciton complex is located in the vicinity of the acceptor. This means that the exciton is bound to the surface-located acceptor. Unlike the acceptor, the donor does not bind the exciton (the binding in this case is negligible). Figure 7c and 7d shows the size dependence of the four lowest exciton energy levels with $|M| = 0$, 1 in the ZnO QDs with

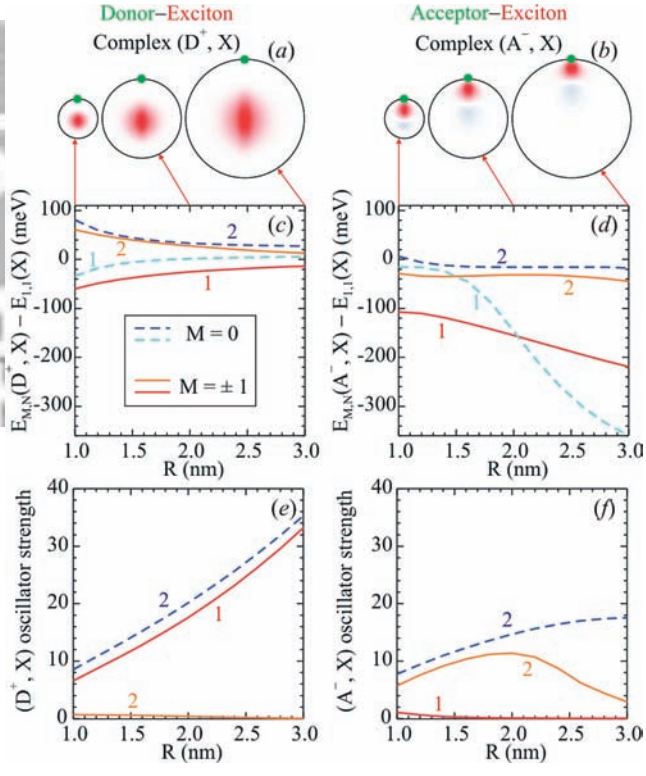

Fig. 7. (a) and (b) Wave functions of exciton center of mass for three ZnO QDs with different sizes. (c) and (d) Lowest energy levels of impurity–exciton complexes counted from the exciton ground-state energy (see Fig. 1). (e) and (f) Corresponding oscillator strengths as a function of the QD radius. Panels (a), (c), (e) and (b), (d), (f) show the calculated results in the presence of a donor and an acceptor, respectively. Large dots show the position of the impurity. Solid (dashed) lines correspond to $|M| = 1$ ($M = 0$).

surface impurities. The energy levels are counted from the ground-state energy of the confined exciton (no impurities). It is seen that the absolute value of the plotted energy difference for the donor-exciton complex is small and decreases with QD size, while this absolute value is much larger and increases with QD size for the acceptor-exciton complex. Such a different behavior of the exciton energy levels is due to the fact that the hole is much heavier than the electron, which makes the surface donor a shallow impurity, while the surface acceptor is a deep impurity. Therefore, excitons can be effectively bound only to surface acceptors.

Figures 7e and 7f show the oscillator strengths of the exciton energy levels from Figs. 7c and 7d. We can see that for the confined excitons and ionized donor–exciton complexes there are two energy levels that have large oscillator strengths (the first level with $|M| = 1$ and the second level with $M = 0$). The energy difference between the two energy levels decreases while their oscillator strengths, which are almost the same for both levels, increase with increasing QD size. On the other hand, the oscillator strength of the ground state of the ionized acceptor–exciton complex is very small and decreases with QD size. Instead, the second energy level, with $|M| = 1$, has large oscillator strength with a maximum for a QD with the radius of about 2 nm.

Summarizing these above observations, one can conclude that the absorption edge, which is defined by the first energy level with $|M| = 1$ for the confined exciton and for the ionized donor–exciton complex and by the second energy level with $|M| = 1$ for the ionized acceptor–exciton complex, depends on the presence of impurities relatively weakly, and it is only few tens of millielectron volts lower in energy for the impurity–exciton complexes than it is for the confined excitons. On the contrary, the position of the UV PL peak, which is defined by the first energy level with $|M| = 1$ for all considered cases, is 100–200 meV lower in energy for the ionized acceptor–exciton complex than it is for the confined exciton or the ionized donor–exciton complex. Some of the fabrication techniques (e.g., wet chemical synthesis[16, 22]) produce ZnO QDs that have the UV PL peak position close to the absorption edge. We can attribute the UV PL in such QDs to confined excitons. The surface of such QDs may contain donors, which only slightly affect the UV PL. Other fabrication techniques, such as wet chemical synthesis in the presence of a polymer,[26] produce ZnO QDs that have the UV PL peak red shifted from the absorption edge as far as a few hundreds of millielectron volts. We argue that this red shift may be caused by the presence of acceptors at the surface of ZnO QDs. The ionized acceptors (e.g., N^-) are more likely to be at the QD surface than inside the QD because the latter fabrication techniques include some type of surface passivation. For example, the method described in Ref. 26 produces ZnO QDs capped with the polyvinyl pyrrolidone (PVP) polymer.

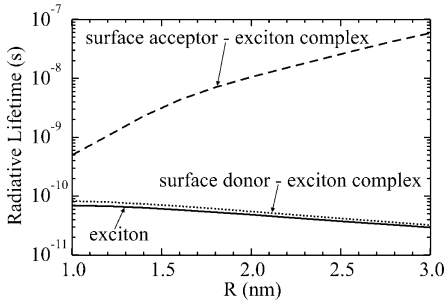

Fig. 8. Radiative lifetime of confined excitons (solid line) and impurity–exciton complexes (dotted and dashed lines) for ZnO QDs as a function of the QD radius. Reprinted with permission from Ref. 30, V. A. Fonoberorov and A. A. Balandin. *Appl. Phys. Lett.*, 85, 5971 (**2004**). © 2004, American Institute of Physics.

In the following, we suggest that the presence of acceptors at the surface of ZnO QDs can be determined by measuring the exciton radiative lifetime. As we mentioned, the radiative recombination lifetime τ of excitons in bulk ZnO is about 322 ps. Figure 8 shows the radiative lifetime as the function of the QD radius for the confined excitons as well as for the impurity–exciton complexes. It is seen that the radiative lifetime of the confined exciton and that of the ionized donor–exciton complex are almost the same; they decrease with QD size and are about an order of magnitude less (for $R \sim 2$ nm) than the bulk exciton lifetime. On the other hand, the radiative lifetime of the ionized acceptor–exciton complex increase with QD size very fast and it is about two orders of magnitude larger (for $R \sim 2$ nm) than bulk exciton lifetime.

Thus, depending on the fabrication technique and ZnO QD surface quality, the origin of UV PL in ZnO QDs is either a recombination of confined excitons or surface-bound ionized acceptor–exciton complexes. In the latter case the Stokes shift on the order of 100–200 meV should be observed in the PL spectrum. The exciton radiative lifetime can be used as a probe of the exciton localization.

4. INTERFACE AND CONFINED OPTICAL PHONONS IN ZINC OXIDE QUANTUM DOTS

It is well known that in QDs with zinc blende crystal structure there exist confined phonon modes with frequencies equal to those of bulk transverse optical (TO) and longitudinal optical (LO) phonons and interface phonon modes with frequencies intermediate between those of TO and LO modes.[31] Interface and confined optical phonon modes have been found for a variety of zinc blende QDs, such as spherical,[31] spheroidal,[32, 33] multilayer spherical,[34] and even multilayer tetrahedral[6] QDs. The calculated frequencies of optical phonon modes have been observed in the Raman, absorption, and PL spectra of zinc blende QDs.[6, 35] Lately, QDs with wurtzite crystal structure, such as ZnO nanostructures, have attracted attention as very

promising candidates for optoelectronic, spintronic, and biological applications. At the same time, only a few reports have addressed the problem of polar optical phonons in wurtzite nanostructures.[36]

The frequencies of optical phonons in small covalent nanocrystals depend on the nanocrystal size because the nanocrystal boundary causes an uncertainty in the phonon wave vector, which results in the red shift and broadening of the phonon peak. While the above size dependence is important for very small covalent nanocrystals, it is negligible in the ionic ZnO QDs with sizes larger than 4 nm. The last is due to the fact that the polar optical phonons in ZnO are almost nondispersive in the region of small wave vectors. Since most of the reported experimental data are for ZnO QDs with sizes larger than 4 nm, in the following we assume that the polar optical phonons are nondispersive in the relevant range of the wave vectors. Due to the uniaxial anisotropy of wurtzite QDs, the confined and interface optical phonon modes in such QDs should be substantially different from those in zinc blende (isotropic) QDs.[36] The main difference comes from the anisotropy of the dielectric function of wurtzite crystals. To describe the dielectric function, we employ the Loudon model, which is widely accepted for the wurtzite nanostructures.[37, 38] For example, the components of the dielectric tensor of wurtzite ZnO are[39]

$$\varepsilon_{\perp}(\omega)=\varepsilon_{\perp}(\infty)\frac{\omega^2-(\omega_{\perp,\mathrm{LO}})^2}{\omega^2-(\omega_{\perp,\mathrm{TO}})^2};\qquad \varepsilon_z(\omega)=\varepsilon_z(\infty)\frac{\omega^2-(\omega_{z,\mathrm{LO}})^2}{\omega^2-(\omega_{z,\mathrm{TO}})^2}, \tag{8}$$

where the optical dielectric constants $\varepsilon_{\perp}(\infty)$ and $\varepsilon_z(\infty)$, LO phonon frequencies $\omega_{\perp,\mathrm{LO}}$ and $\omega_{z,\mathrm{LO}}$, and TO phonon frequencies $\omega_{\perp,\mathrm{TO}}$ and $\omega_{z,\mathrm{TO}}$ of bulk wurtzite ZnO are taken from Ref. 40. The components of the dielectric tensor of some ternary wurtzite crystals, such as $Mg_xZn_{1-x}O$ ($x<0.33$), have more complex frequency dependence[41]:

$$\varepsilon_{\perp}(\omega)=\varepsilon_{\perp}(\infty)\frac{\omega^2-(\omega_{\perp1,\mathrm{LO}})^2}{\omega^2-(\omega_{\perp1,\mathrm{TO}})^2}\,\frac{\omega^2-(\omega_{\perp2,\mathrm{LO}})^2}{\omega^2-(\omega_{\perp2,\mathrm{TO}})^2};\qquad \varepsilon_z(\omega)=\varepsilon_z(\infty)\frac{\omega^2-(\omega_{z,\mathrm{LO}})^2}{\omega^2-(\omega_{z,\mathrm{TO}})^2}. \tag{9}$$

The corresponding material parameters from Eq. (9) for bulk wurtzite $Mg_{0.2}Zn_{0.8}O$ are also taken from Ref. 40. Zone center optical phonon frequencies of wurtzite ZnO and $Mg_{0.2}Zn_{0.8}O$ are shown in Figure 9. Since there are only two zone center optical phonon frequencies (one LO and one TO) in zinc blende crystals, the phonon band structure of wurtzite crystals is more complex than that of zinc blende crystals. It is shown in the following that the last fact leads to polar optical phonon modes in wurtzite QDs that are strongly different from those in zinc blende QDs.

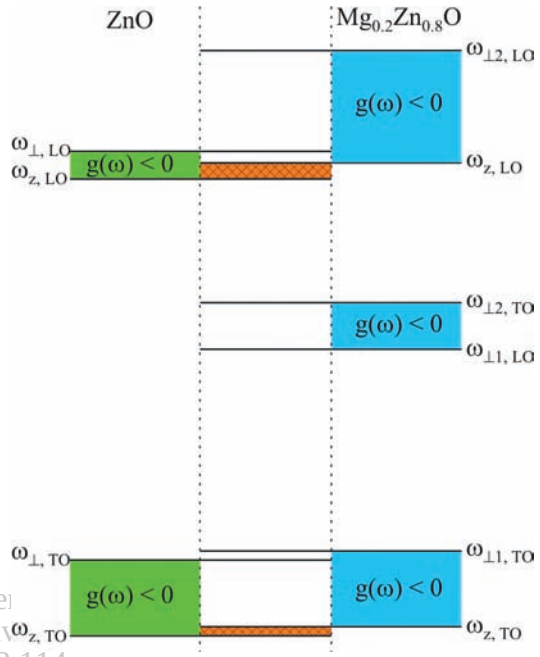

Fig. 9. Zone center optical phonon frequencies of ZnO and $Mg_{0.2}Zn_{0.8}O$. Shaded regions correspond to the condition $g(\omega)<0$ [see Eq. (22)]. Cross-hatched regions correspond to the condition $g(\omega)<0$ for ZnO and $g(\omega)>0$ for $Mg_{0.2}Zn_{0.8}O$.

The description of the interface and confined polar optical phonons in this section mostly follows our derivation given in Refs. 36 and 40. First, we present the analytical derivation of the polar optical phonon modes in spheroidal QDs with wurtzite crystal structure. Then, we apply our theory to a freestanding spheroidal ZnO QD and to a spheroidal ZnO QD embedded into a $Mg_{0.2}Zn_{0.8}O$ crystal.

Let us consider a spheroidal QD with wurtzite crystal structure and with semiaxes a and c. The coordinate system (x, y, z') is chosen in such a way that the semiaxis c is directed along the symmetry axis z' of the QD. The equation of the QD surface is

$$\frac{x^2+y^2}{a^2}+\frac{z'^2}{c^2}=1. \tag{10}$$

After we introduce a new coordinate z such as

$$z'=\frac{c}{a}z \tag{11}$$

and transform the new Cartesian coordinates (x, y, z) into spherical coordinates (r, θ, ϕ), Eq. (10) of the QD surface becomes $r=a$. In the following description, we assume that the QD (medium $k=1$) is embedded in a wurtzite crystal (medium $k=2$). A freestanding QD can be easily considered as a special case.

Within the framework of the dielectric-continuum approximation, the potential $V(\mathbf{r})$ of polar optical phonons

satisfies Maxwell's equation, which can be written in the coordinates $\mathbf{r} = (x, y, z)$ as

$$-\nabla(\hat{\varepsilon}(\omega, \mathbf{r})\nabla V(\mathbf{r})) = 0 \tag{12}$$

with the dielectric tensor $\hat{\varepsilon}(\omega, \mathbf{r})$ defined as

$$\hat{\varepsilon}(\omega, \mathbf{r}) = \begin{pmatrix} \varepsilon_\perp(\omega, \mathbf{r}) & 0 & 0 \\ 0 & \varepsilon_\perp(\omega, \mathbf{r}) & 0 \\ 0 & 0 & \frac{a^2}{c^2}\varepsilon_z(\omega, \mathbf{r}) \end{pmatrix}. \tag{13}$$

Note that the term a^2/c^2 appears in Eq. (13) due to the coordinate transformation (11). The dielectric tensor (13) is constant in both media:

$$\hat{\varepsilon}(\omega, \mathbf{r}) = \begin{cases} \hat{\varepsilon}_1(\omega), & r \le a; \\ \hat{\varepsilon}_2(\omega), & r > a, \end{cases} \tag{14}$$

therefore it is convenient to split Eq. (12) into separate equations for each medium:

$$-\nabla(\hat{\varepsilon}_k(\omega)\nabla V_k(\mathbf{r})) = 0; \qquad k = 1, 2 \tag{15}$$

and apply the corresponding boundary conditions:

$$V_1(a, \theta, \phi) = V_2(a, \theta, \phi); \tag{16}$$

$$D_1(a, \theta, \phi) = D_2(a, \theta, \phi), \tag{17}$$

where the projections of the displacement vector $\mathbf{D}$ on the outer normal $\mathbf{n}$ at the QD surface can be written as

$$D_k(a, \theta, \phi) = (\mathbf{n}(\mathbf{r})\hat{\varepsilon}_k(\omega)\nabla V_k(\mathbf{r}))|_{r=a}; \qquad k = 1, 2. \tag{18}$$

The phonon potential $V_1(\mathbf{r})$ that satisfies Eq. (15) and is finite everywhere inside the QD can be found analytically in spheroidal coordinates (ξ_1, η_1, ϕ):

$$V_1(\mathbf{r}) = \frac{P_l^m(\xi_1)}{P_l^m(\xi_1^{(0)})} P_l^m(\eta_1)\, e^{im\phi}. \tag{19}$$

Analogously, the phonon potential $V_2(\mathbf{r})$ that satisfies Eq. (15) and vanishes far away from the QD can be found analytically in spheroidal coordinates (ξ_2, η_2, ϕ):

$$V_2(\mathbf{r}) = \frac{Q_l^m(\xi_2)}{Q_l^m(\xi_2^{(0)})} P_l^m(\eta_2)\, e^{im\phi}. \tag{20}$$

In Eqs. (19) and (20), P_l^m and Q_l^m are associated Legendre functions of the first and second kinds, respectively; the integers l ($l \ge 0$) and m ($|m| \le l$) are quantum numbers of the phonon mode. The spheroidal coordinates (ξ_k, η_k) are related to the spherical coordinates (r, θ) as

$$\begin{cases} r\sin\theta = a\sqrt{\left(\frac{1}{g_k(\omega)} - 1\right)(\xi_k^2 - 1)}\,\sqrt{1 - \eta_k^2}, \\ r\cos\theta = a\sqrt{1 - g_k(\omega)}\,\xi_k\,\eta_k, \end{cases} \tag{21}$$

where $k = 1, 2$ and

$$g_k(\omega) = \frac{a^2}{c^2}\frac{\varepsilon_z^{(k)}(\omega)}{\varepsilon_\perp^{(k)}(\omega)}. \tag{22}$$

The range of the spheroidal coordinate η_k is $-1 \le \eta_k \le 1$. Depending on the value of the function (22), the spheroidal coordinate ξ_k can have the following range:

$$\begin{array}{lll} 0 < \xi_k < 1 & \text{if} & g_k(\omega) < 0; \\ \xi_k > 1 & \text{if} & 0 < g_k(\omega) < 1; \\ \mathrm{i}\xi_k > 0 & \text{if} & g_k(\omega) > 1. \end{array} \tag{23}$$

According to Eq. (21), the QD surface $r = a$ is defined in the spheroidal coordinates as

$$\begin{cases} \xi_k = \xi_k^{(0)} \equiv 1/\sqrt{1 - g_k(\omega)}, \\ \eta_k = \cos\theta. \end{cases} \tag{24}$$

Therefore, the part of the phonon potential $V_1(\mathbf{r})$ defined by Eq. (19) and the part of the phonon potential $V_2(\mathbf{r})$ defined by Eq. (20) coincide at the QD surface. Thus, the first boundary condition, given by Eq. (16), is satisfied.

Now, let us find the normal component of the displacement vector $\mathbf{D}$ at the QD surface. According to Eq. (18),

$$D_k(a, \theta, \phi) = \varepsilon_\perp^{(k)}(\omega)\left[(g_k(\omega)\cos^2\theta + \sin^2\theta)\left.\frac{\partial V_k}{\partial r}\right|_{r=a} + \frac{1 - g_k(\omega)}{a}\sin\theta\cos\theta\left.\frac{\partial V_k}{\partial\theta}\right|_{r=a}\right]. \tag{25}$$

Using relation (21) between the coordinates (ξ_k, η_k) and (r, θ), we can calculate each of the two partial derivatives from Eq. (25):

$$\left.\frac{\partial V_k}{\partial r}\right|_{r=a} = \frac{1}{a(g_k(\omega)\cos^2\theta + \sin^2\theta)} \times \left[\frac{g_k(\omega)}{\sqrt{1 - g_k(\omega)}}\left.\frac{\partial V_k}{\partial \xi_k}\right|_{\substack{\xi_k = \xi_k^{(0)} \\ \eta_k = \cos\theta}} + \cos\theta\sin^2\theta(1 - g_k(\omega))\left.\frac{\partial V_k}{\partial \eta_k}\right|_{\substack{\xi_k = \xi_k^{(0)} \\ \eta_k = \cos\theta}}\right], \tag{26}$$

$$\left.\frac{\partial V_k}{\partial \theta}\right|_{r=a} = -\sin\theta \left.\frac{\partial V_k}{\partial \eta_k}\right|_{\substack{\xi_k=\xi_k^{(0)} \\ \eta_k=\cos\theta}}. \quad (27)$$

Substituting Eqs. (27) and (28) into Eq. (25), one obtains a simple formula:

$$D_k(a,\theta,\phi) = \frac{\varepsilon_\perp^{(k)}(\omega) g_k(\omega)}{a\sqrt{1-g_k(\omega)}} \left.\frac{\partial V_k}{\partial \xi_k}\right|_{\substack{\xi_k=\xi_k^{(0)} \\ \eta_k=\cos\theta}}. \quad (28)$$

Finally, using the explicit form of the phonon potentials (19) and (20) as well as Eqs. (22) and (24), one can rewrite Eq. (28) as

$$D_1(a,\theta,\phi) = \frac{a}{c^2}\frac{\varepsilon_z^{(1)}(\omega)}{\sqrt{1-g_1(\omega)}} \left.\frac{d\ln P_l^m(\xi_1)}{d\xi_1}\right|_{\xi_1=\xi_1^{(0)}} \times P_l^m(\cos\theta)\, e^{im\phi}; \quad (29)$$

$$D_2(a,\theta,\phi) = \frac{a}{c^2}\frac{\varepsilon_z^{(2)}(\omega)}{\sqrt{1-g_2(\omega)}} \left.\frac{d\ln Q_l^m(\xi_2)}{d\xi_2}\right|_{\xi_2=\xi_2^{(0)}} \times P_l^m(\cos\theta)\, e^{im\phi}. \quad (30)$$

Substituting Eqs. (29) and (30) into the second boundary condition (17), one can see that it is satisfied only when the following equality is true:

$$\varepsilon_z^{(1)}(\omega)\left(\xi\frac{d\ln P_l^m(\xi)}{d\xi}\right)\Bigg|_{\xi=1/\sqrt{1-g_1(\omega)}} = \varepsilon_z^{(2)}(\omega)\left(\xi\frac{d\ln Q_l^m(\xi)}{d\xi}\right)\Bigg|_{\xi=1/\sqrt{1-g_2(\omega)}}. \quad (31)$$

Thus, we have found the equation that defines the spectrum of polar optical phonons in a wurtzite spheroidal QD embedded in a wurtzite crystal. Note that Eq. (31) can also be obtained using a completely different technique developed by us for wurtzite nanocrystals of arbitrary shape.[36] It should be pointed out that, for a spheroidal QD with zinc blende crystal structure, $\varepsilon_\perp^{(k)}(\omega) = \varepsilon_z^{(k)}(\omega) \equiv \varepsilon^{(k)}(\omega)$, and Eq. (31) reduces to the one obtained in Refs. 32 and 33. The fact that the spectrum of polar optical phonons does not depend on the absolute size of a QD[31, 32] is also seen from Eq. (31).

The case of a freestanding QD is no less important for practical applications. In this case, the dielectric tensor of the exterior medium is a constant $\varepsilon_D \equiv \varepsilon_z^{(2)}(\omega) = \varepsilon_\perp^{(2)}(\omega)$. Therefore, using the explicit form of associated Legendre polynomials P_l^m and omitting the upper index (1) in the components of the dielectric tensor of the QD, we can represent Eq. in the following convenient form:

$$\sum_{n=0}^{\left[\frac{l-|m|}{2}\right]}\left[\frac{c^2}{a^2}\frac{\varepsilon_\perp(\omega)}{\varepsilon_D}|m| + \frac{\varepsilon_z(\omega)}{\varepsilon_D}(l-|m|-2n) - f_l^{|m|}\left(\frac{a}{c}\right)\right] \times \binom{l-|m|}{2n}\frac{(2n-1)!!\,(2l-2n-1)!!}{(2l-1)!!} \times \left[\frac{a^2}{c^2}\frac{\varepsilon_z(\omega)}{\varepsilon_\perp(\omega)} - 1\right]^n = 0, \quad (32)$$

where

$$f_l^m(\alpha) = \xi\left.\frac{d\ln Q_l^m(\xi)}{d\xi}\right|_{\xi=1/\sqrt{1-\alpha^2}}. \quad (33)$$

It can be shown that the function $f_l^m(\alpha)$ increases monotonely from $-\infty$ to 0 when α increases from 0 to ∞. As seen from Eq. (32), there are no phonon modes with $l=0$, and all phonon frequencies with $m \neq 0$ are twice degenerate with respect to the sign of m. For a spherical ($\alpha = 1$) freestanding QD, one has to take the limit $\xi \to \infty$ in Eq. (33), which results in $f_l^m(1) = -(l+1)$. Thus, in the case of a zinc blende spherical QD [$\varepsilon_\perp(\omega) = \varepsilon_z(\omega) \equiv \varepsilon(\omega)$; $a=c$], Eq. (32) gives the well-known equation $\varepsilon(\omega)/\varepsilon_D = -1 - 1/l$ derived in Ref. 31.

Now, let us consider freestanding spheroidal ZnO QDs and examine the phonon modes with quantum numbers $l=1$, 2, 3, 4 and $m=0$, 1. The components of the dielectric tensor of wurtzite ZnO are given by Eq. (8). The exterior medium is considered to be air with $\varepsilon_D = 1$. Figure 10a shows the spectrum of polar optical phonons with $m=0$, and Figure 10b shows the spectrum of polar optical phonons with $m=1$. The frequencies with even l are plotted with solid curves, while the frequencies with odd l are plotted with dashed curves. The frequencies in Figure 10 are found as solutions of Eq. 32 and are plotted as a function of the ratio of the spheroidal semiaxes a and c. Thus, in the leftmost part of the plots we have the phonon spectrum for a spheroid degenerated into a vertical line segment. Farther to the right, we have the spectrum for prolate spheroids. In the central part of the plots, we have the phonon spectrum for a sphere. Farther on, we have the spectrum for oblate spheroids; and in the rightmost part of the plots, we have the phonon spectrum for a spheroid degenerated into a horizontal flat disk.

The calculated spectrum of phonons in the freestanding ZnO QDs can be divided into three regions: confined TO phonons ($\omega_{z,\mathrm{TO}} < \omega < \omega_{\perp,\mathrm{TO}}$), interface phonons ($\omega_{\perp,\mathrm{TO}} < \omega < \omega_{z,\mathrm{LO}}$), and confined LO phonons ($\omega_{z,\mathrm{LO}} < \omega < \omega_{\perp,\mathrm{LO}}$). The division into confined and interface phonons is based on the sign of the function $g(\omega)$ [see Eq. (22)]. We call the phonons with eigenfrequency ω interface phonons if

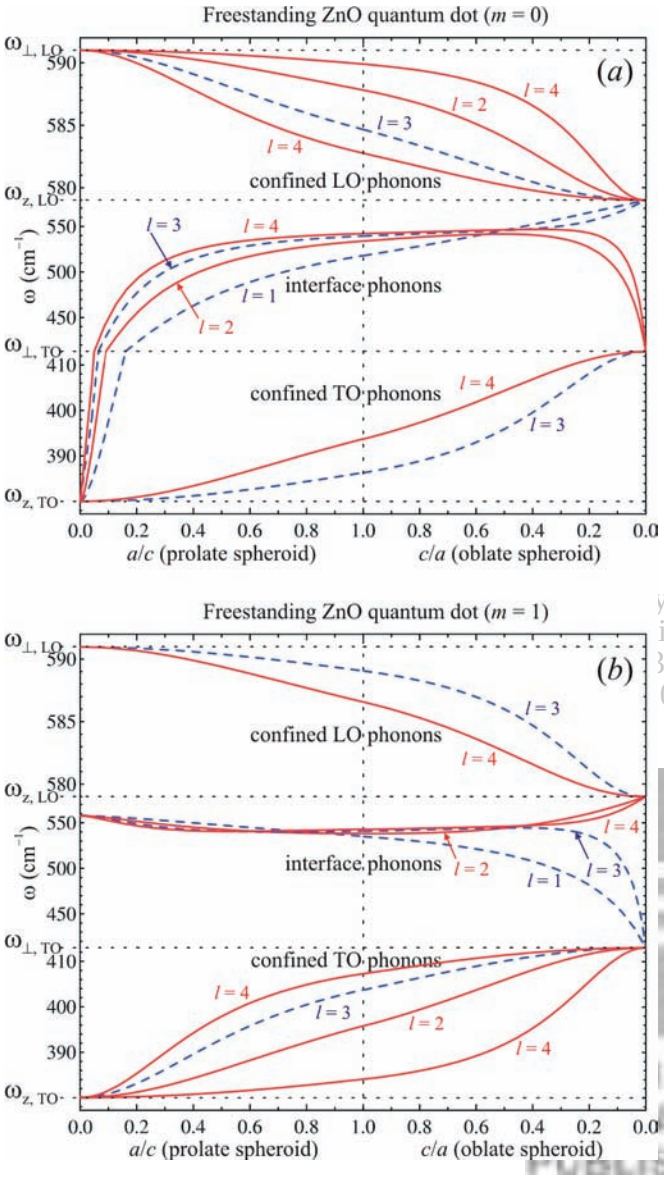

Fig. 10. Frequencies of polar optical phonons with $l = 1, 2, 3, 4$ and $m = 0$ (a) or $m = 1$ (b) for a freestanding spheroidal ZnO QD as a function of the ratio of spheroidal semiaxes. Solid curves correspond to phonons with even l, and dashed curves correspond to phonons with odd l. Frequency scale is different for confined TO, interface, and confined LO phonons.

$g(\omega) > 0$ and confined phonons if $g(\omega) < 0$. To justify the classification of phonon modes as interface and confined ones based on the sign of the function $g_1(\omega)$, let us consider the phonon potential (19) inside the QD. If $g_1(\omega) < 0$, then according to Eq. (23), $0 < \xi_1 < 1$; therefore, $P_l^m(\xi_1)$ is an oscillatory function of ξ_1, and the phonon potential (19) is mainly confined inside the QD. On the contrary, if $g_1(\omega) > 0$, then according to Eq. (23), $\xi_1 > 1$ or $i\xi_1 > 0$; therefore, $P_l^m(\xi_1)$ increases monotonely with ξ_1 as ξ_1^l, reaching the maximum at the QD surface together with the phonon potential (19). Note that vertical frequency scale in Figure 10 is different for confined TO, interface, and confined LO phonons. The true scale is shown in Figure 9.

Analyzing Eq. (32), one can find that for each pair (l, m) there is one interface optical phonon and $l - |m|$ confined optical phonons for $m \neq 0$ ($l - 1$ for $m = 0$). Therefore, we can see four interface phonons and six confined phonons for both $m = 0$ and $m = 1$ in Figure 10. However, one can see that there are four confined LO phonons with $m = 0$ and only two confined LO phonons with $m = 1$. On the contrary, there are only two confined TO phonons with $m = 0$ and four confined TO phonons with $m = 1$ in Figure 10.

When the shape of the spheroidal QD changes from the vertical line segment to the horizontal flat disk, the frequencies of all confined LO phonons decrease from $\omega_{\perp,\mathrm{LO}}$ to $\omega_{z,\mathrm{LO}}$. At the same time, the frequencies of all confined TO phonons increase from $\omega_{z,\mathrm{TO}}$ to $\omega_{\perp,\mathrm{TO}}$. It is also seen from Figure 10 that, for very small ratios a/c, which is the case for so-called quantum rods, the interface phonons with $m = 0$ become confined TO phonons, while the frequencies of all interface phonons with $m = 1$ degenerate into a single frequency. When the shape of the spheroidal QD changes from the vertical line segment to the horizontal flat disk, the frequencies of interface phonons with odd l and $m = 0$ increase from $\omega_{z,\mathrm{TO}}$ to $\omega_{z,\mathrm{LO}}$, while the frequencies of interface phonons with even l and $m = 0$ increase for prolate spheroids starting from $\omega_{z,\mathrm{TO}}$, like for the phonons with odd l, but they further decrease up to $\omega_{\perp,\mathrm{TO}}$ for oblate spheroids. On the contrary, when the shape of the spheroidal QD changes from the vertical line segment to the horizontal flat disk, the frequencies of interface phonons with odd l and $m = 1$ decrease from a single interface frequency to $\omega_{\perp,\mathrm{TO}}$, while the frequencies of interface phonons with even l and $m = 1$ decrease for prolate spheroids starting from a single frequency, like for the phonons with odd l, but they further increase up to $\omega_{z,\mathrm{LO}}$ for oblate spheroids.

In the following, we study phonon potentials corresponding to the polar optical phonon modes with $l = 1$, 2, 3, 4 and $m = 0$. In Figure 11, we present the phonon potentials for a spherical freestanding ZnO QD. The phonon potentials for QDs with arbitrary spheroidal shapes can be found analogously using Eqs. (19) and (20) and the coordinate transformation (11). As seen from Figure 11, the confined LO phonons are indeed confined inside the QD. However, unlike confined phonons in zinc blende QDs, confined phonons in wurtzite QDs slightly penetrate into the exterior medium. The potential of interface phonon modes is indeed localized near the surface of the wurtzite QD. While there are no confined TO phonons in zinc blende QDs, they appear in wurtzite QDs. It is seen from Figure 11 that confined TO phonons are indeed localized mainly inside the QD. However, they penetrate into the exterior medium much stronger than confined LO phonons.

Figure 12 shows the calculated spectrum of polar optical phonons with $l = 1$, 2, 3, 4 and $m = 0$ in a spherical wurtzite ZnO QD as a function of the optical dielectric

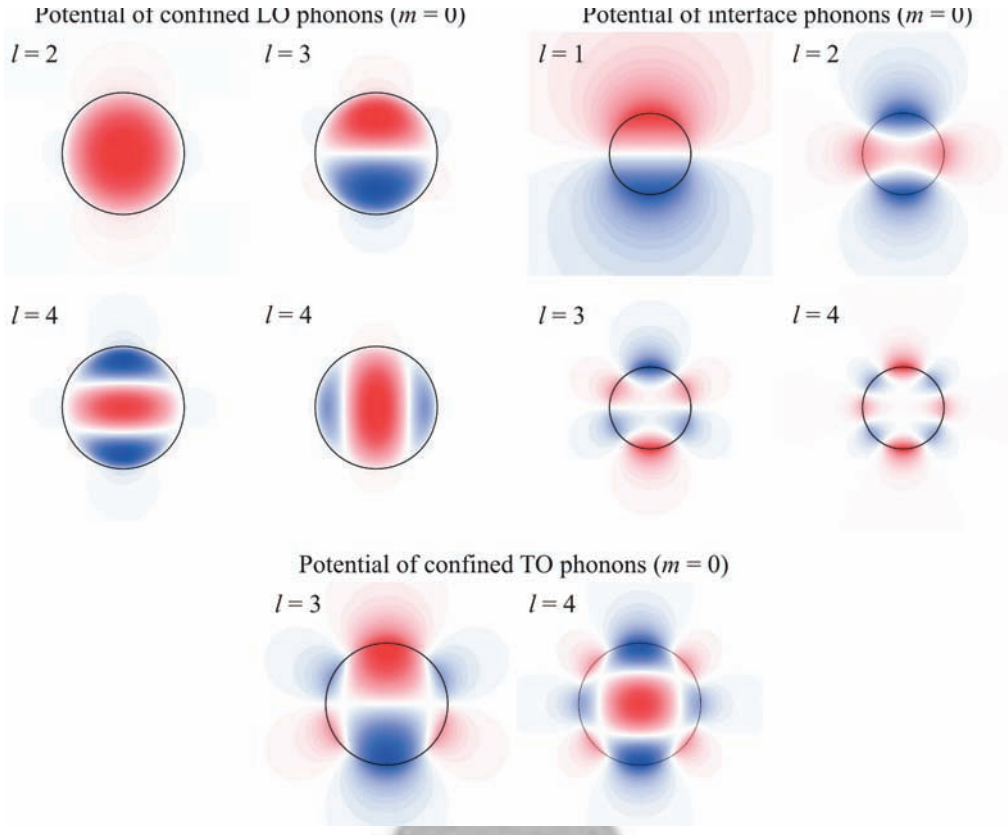

Fig. 11. Cross sections of phonon potentials corresponding to polar optical phonon modes with $l = 1, 2, 3, 4$ and $m = 0$ for the freestanding spherical ZnO QDs. *Z*-axis is directed vertically. Blue and red colors denote negative and positive values of phonon potentials, correspondingly. Black circle represents the QD surface.

constant of the exterior medium ε_D. It is seen from Figure 12 that the frequencies of interface optical phonons decrease substantially when ε_D changes from the vacuum's value ($\varepsilon_D = 1$) to the ZnO nanocrystal's value ($\varepsilon_D = 3.7$). At the same time, the frequencies of confined optical phonons decrease only slightly with ε_D.

Using the theory of excitonic states in wurtzite QDs, it can be shown that the dominant component of the wave function of the exciton ground state in spheroidal ZnO QDs is symmetric with respect to the rotations around the z-axis or reflection in the xy-plane. Therefore, the selection rules for the polar optical phonon modes observed in the resonant Raman spectra of ZnO QDs are $m = 0$ and $l = 2, 4, 6, \ldots$. The phonon modes with higher symmetry (smaller quantum number l) are more likely to be observed in the Raman spectra. It is seen from Figure 11 that the confined LO phonon mode with $l = 2$, $m = 0$ and the confined TO mode with $l = 4$, $m = 0$ are the confined modes with the highest symmetry among the confined LO and TO phonon modes, correspondingly. Therefore, they should give the main contribution to the resonant Raman spectrum of spheroidal ZnO QDs.

In fact, the above conclusion has an experimental confirmation. In the resonant Raman spectrum of spherical ZnO QDs with diameter 8.5 nm from Ref. 42, the main Raman peak in the region of LO phonons has the frequency 588 cm^{-1}, and the main Raman peak in the region of TO phonons has the frequency 393 cm^{-1} (see large dots in Fig. 12). In accordance with Figure 12, our calculations give the frequency 587.8 cm^{-1} of the confined LO phonon mode with $l = 2$, $m = 0$ and the frequency 393.7 cm^{-1} of the confined TO phonon mode with $l = 4$, $m = 0$. This excellent agreement of the experimental and calculated frequencies allows one to predict the main peaks in the LO and TO regions of a Raman spectra of spheroidal ZnO QDs using the corresponding curves from Figure 10.

It is illustrative to consider spheroidal ZnO QDs embedded into an $Mg_{0.2}Zn_{0.8}O$ crystal. The components of the dielectric tensors of wurtzite ZnO and $Mg_{0.2}Zn_{0.8}O$ are given by Eqs. (8) and (9), correspondingly. The relative position of optical phonon bands of wurtzite ZnO and $Mg_{0.2}Zn_{0.8}O$ is shown in Figure 9. It is seen from Eq. (22) that $g_1(\omega) < 0$ inside the shaded region corresponding to ZnO in Figure 9 and $g_2(\omega) < 0$ inside the shaded region corresponding to $Mg_{0.2}Zn_{0.8}O$. As it has been shown, the frequency region where $g_1(\omega) < 0$ corresponds to confined phonons in a freestanding spheroidal ZnO QD. However, there can be no confined phonons in the host $Mg_{0.2}Zn_{0.8}O$ crystal. Indeed, there are no physical solutions of Eq. (31)

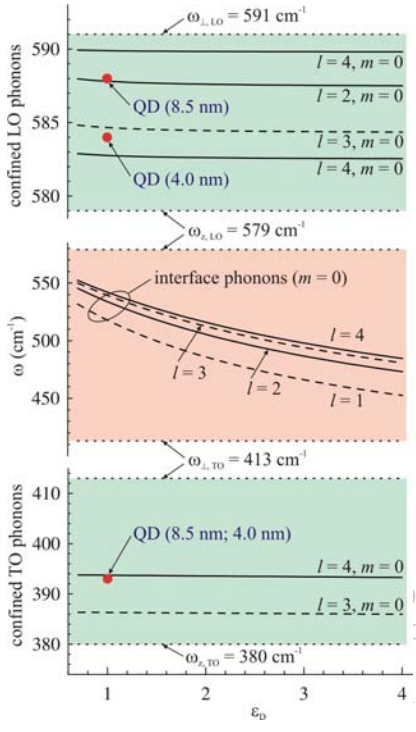

Fig. 12. Spectrum of several polar optical phonon modes in spherical wurtzite ZnO nanocrystals as a function of the optical dielectric constant of the exterior medium. Note that the scale of frequencies is different for confined LO, interface, and confined TO phonons. Large red dots show the experimental points from Ref. 42.

when $g_2(\omega) < 0$. The solutions of Eq. (31) are nonphysical in this case because the spheroidal coordinates (ξ_2, η_2) defined by Eq. (21) cannot cover the entire space outside the QD. If we allow the spheroidal coordinates (ξ_2, η_2) to be complex, then the phonon potential outside the QD becomes complex and diverges logarithmically when $\xi_2 = 1$; the latter is clearly nonphysical. It can be also shown that Eq. (31) does not have any solutions when $g_1(\omega) > 0$ and $g_2(\omega) > 0$. Therefore, the only case when Eq. (31) allows for physical solutions is $g_1(\omega) < 0$ and $g_2(\omega) > 0$. The frequency regions that satisfy the latter condition are cross-hatched in Figure 9. There are two such regions: $\omega^{(1)}_{z,\mathrm{TO}} < \omega < \omega^{(2)}_{z,\mathrm{TO}}$ and $\omega^{(1)}_{z,\mathrm{LO}} < \omega < \omega^{(2)}_{z,\mathrm{LO}}$, which are further called the regions of TO and LO phonons, respectively.

Let us now examine the LO and TO phonon modes with quantum numbers $l = 1, 2, 3, 4$ and $m = 0, 1$. Figure 13a shows the spectrum of polar optical phonons with $m = 0$, and Figure 13b shows the spectrum of polar optical phonons with $m = 1$. The frequencies with even l are plotted with solid curves, while the frequencies with odd l are plotted with dashed curves. The frequencies in Figure 13 are found as solutions of Eq. (31) and are plotted as a function of the ratio of the spheroidal semiaxes a and c, similar to Figure 10 for the freestanding spheroidal ZnO QD. Note that vertical frequency scale in Figure 13 is different for TO phonons and LO phonons. The true scale is shown in Figure 9.

Comparing Figure 13a with Figure 10a and Figure 13b with Figure 10b, we can see the similarities and distinctions in the phonon spectra of the ZnO QD embedded into the $Mg_{0.2}Zn_{0.8}O$ crystal and that of the freestanding ZnO QD. For a small ratio a/c, we have the same number of TO phonon modes with the frequencies originating from $\omega^{(1)}_{z,\mathrm{TO}}$ for the embedded and freestanding ZnO QDs. With the increase of the ratio a/c, the frequencies of TO phonons increase for both embedded and freestanding ZnO QDs, but the number of TO phonon modes gradually decreases in the embedded ZnO QD. When $a/c \to \infty$, only two phonon modes with odd l are left for $m = 0$, and two phonon modes with even l are left for $m = 1$. The frequencies of these phonon modes increase up to $\omega^{(2)}_{z,\mathrm{TO}}$ when $a/c \to \infty$. However, for this small ratio c/a, we have the same number of LO phonon modes with the frequencies originating from $\omega^{(1)}_{z,\mathrm{LO}}$ for the embedded and freestanding ZnO QDs. With the increase of the ratio c/a, the

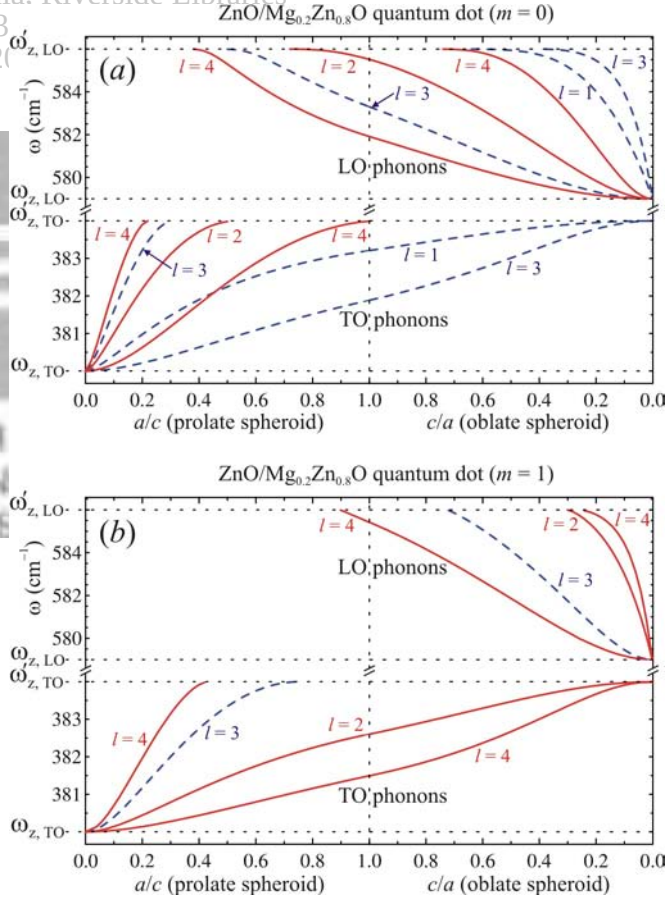

Fig. 13. Frequencies of polar optical phonons with $l = 1, 2, 3, 4$ and $m = 0$ (a) or $m = 1$ (b) for a spheroidal ZnO/$Mg_{0.2}Zn_{0.8}O$ QD as a function of the ratio of spheroidal semiaxes. Solid curves correspond to phonons with even l, and dashed curves correspond to phonons with odd l. Frequency scale is different for TO and LO phonons. Frequencies $\omega_{z,\mathrm{TO}}$ and $\omega_{z,\mathrm{LO}}$ correspond to ZnO, and frequencies $\omega'_{z,\mathrm{TO}}$ and $\omega'_{z,\mathrm{LO}}$ correspond to $Mg_{0.2}Zn_{0.8}O$.

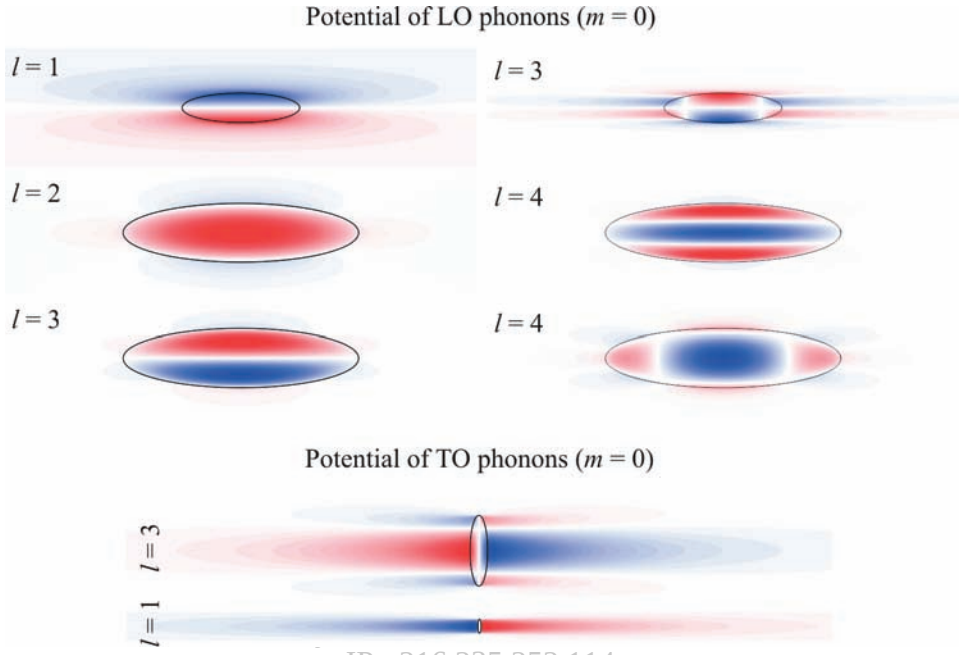

Fig. 14. Cross sections of phonon potentials corresponding to polar optical phonon modes with $l = 1, 2, 3, 4$ and $m = 0$ for the oblate spheroidal ZnO/$Mg_{0.2}Zn_{0.8}O$ QDs with aspect ratio 1/4. *Z*-axis is directed vertically. Blue and red colors denote negative and positive values of phonon potentials, correspondingly. Black ellipse represents the QD surface.

frequencies of all LO phonons increase for the embedded ZnO QD, and the number of such phonons gradually decreases. When $c/a \to \infty$, there are no phonons left for the embedded ZnO QD. At the same time, for the free-standing ZnO QD, with the increase of the ratio c/a, the frequencies of two LO phonons with odd l and $m = 0$ and two LO phonons with even l and $m = 1$ decrease and go into the region of interface phonons.

It is seen from the preceding paragraph that for the ZnO QD with a small ratio c/a embedded into the $Mg_{0.2}Zn_{0.8}O$ crystal the two LO and two TO phonon modes with odd l and $m = 0$ and with even l and $m = 1$ may correspond to interface phonons. To check this hypothesis, we further studied phonon potentials corresponding to the polar optical phonon modes with $l = 1, 2, 3, 4$ and $m = 0$. In Figure 14, we present the phonon potentials for the spheroidal ZnO QD with the ratio $c/a = 1/4$ embedded into the $Mg_{0.2}Zn_{0.8}O$ crystal. The considered ratio $c/a = 1/4$ of the spheroidal semiaxes is a reasonable value for epitaxial ZnO/$Mg_{0.2}Zn_{0.8}O$ QDs. It is seen in Figure 14 that the LO phonon with $l = 1$, one of the LO phonons with $l = 3$, and all two TO phonons are indeed interface phonons since they achieve their maximal and minimal values at the surface of the ZnO QD. It is interesting that the potential of interface TO phonons is strongly extended along the *z*-axis, while the potential of interface LO phonons is extended in the *xy*-plane. All other LO phonons in Figure 14 are confined. The most symmetrical phonon mode is, again, the one with $l = 2$ and $m = 0$. Therefore, it should give the main contribution to the Raman spectrum of oblate spheroidal ZnO QDs embedded into the $Mg_{0.2}Zn_{0.8}O$ crystal. Unlike for free-standing ZnO QDs, no pronounced TO phonon peaks are expected for the embedded ZnO QDs.

5. RAMAN SPECTRA OF ZINC OXIDE QUANTUM DOTS

Both resonant and nonresonant Raman scattering spectra have been measured for ZnO QDs. Due to the wurtzite crystal structure of bulk ZnO, the frequencies of both LO and TO phonons are split into two frequencies with symmetries A_1 and E_1. In ZnO, in addition to LO and TO phonon modes, there are two nonpolar Raman active phonon modes with symmetry E_2. The low-frequency E_2 mode is associated with the vibration of the heavy Zn sublattice, while the high-frequency E_2 mode involves only the oxygen atoms. The Raman spectra of ZnO nanostructures always show shift of the bulk phonon frequencies.[24, 42] The origin of this shift, its strength, and dependence on the QD diameter are still the subjects of debate. Understanding the nature of the observed shift is important for interpretation of the Raman spectra and understanding properties of ZnO nanostructures.

In the following, we present data that clarify the origin of the peak shift. There are three main mechanisms that can induce phonon peak shifts in ZnO nanostructures: (1) spatial confinement within the QD boundaries; (2) phonon localization by defects (oxygen deficiency, zinc excess, surface impurities, etc.); or (3) laser-induced heating in nanostructure ensembles. Usually, only the first

mechanism, referred to as optical phonon confinement, is invoked as an explanation for the phonon frequency shifts in ZnO nanostructures.[42]

The optical phonon confinement was originally introduced to explain the observed frequency shift in small covalent semiconductor nanocrystals. It attributes the red shift and broadening of the Raman peaks to the relaxation of the phonon wave vector selection rule due to the finite size of the nanocrystals.[43] It has been recently shown theoretically by us[36,40] that, while this phenomenological model is justified for small covalent nanocrystals, it cannot be applied to ionic ZnO QDs with the sizes larger than 4 nm. The last is due to the fact that the polar optical phonons in ZnO are almost nondispersive in the region of small wave vectors. In addition, the asymmetry of the wurtzite crystal lattice leads to the QD shape-dependent splitting of the frequencies of polar optical phonons in a series of discrete frequencies. Here, we argue that all three aforementioned mechanisms contribute to the observed peak shift in ZnO nanostructures, and that in many cases, the contribution of the optical phonon confinement can be relatively small compared to other mechanisms.

We carried out systematic nonresonant and resonant Raman spectroscopy of ZnO QDs with a diameter of 20 nm together with the bulk reference sample. The experimental Raman spectroscopy data for ZnO QDs presented in this section are mostly taken from a study reported by Alim, Fonoberov, and Balandin.[44] To elucidate the effects of heating, we varied the excitation laser power over a wide range. The reference wurtzite bulk ZnO crystal (University Wafers) had dimensions $5 \times 5 \times 0.5\,\mathrm{mm}^3$ with *a*-plane (11–20) facet. The investigated ZnO QDs were produced by the wet chemistry method. The dots had nearly spherical shape with an average diameter of 20 nm and good crystalline structure, as evidenced by the TEM study. The purity of ZnO QDs in a powder form was 99.5%. A Renishaw micro-Raman spectrometer 2000 with visible (488-nm) and UV (325-nm) excitation lasers was employed to measure the nonresonant and resonant Raman spectra of ZnO, respectively. The number of gratings in the Raman spectrometer was 1800 for visible laser and 3000 for UV laser. All spectra were taken in the backscattering configuration.

The nonresonant and resonant Raman spectra of bulk ZnO crystal and ZnO QD sample are shown in Figures 15 and 16, respectively. A compilation of the reported frequencies of Raman active phonon modes in bulk ZnO gives the phonon frequencies 102, 379, 410, 439, 574 cm, and 591 cm^{-1} for the phonon modes E_2(low), A_1(TO), E_1(TO), E_2(high), A_1(LO), and E1(LO), correspondingly.[44] In our spectrum from the bulk ZnO, the peak at 439 cm^{-1} corresponds to E_2(high) phonon, while the peaks at 410 and 379 cm^{-1} correspond to E_1(TO) and A_1(TO) phonons, respectively. No LO phonon peaks are seen in the spectrum of bulk ZnO. On the contrary, no TO phonon peaks are seen in the Raman spectrum of ZnO QDs. In the QD spectrum, the LO phonon peak at 582 cm^{-1} has a frequency intermediate between those of A_1(LO) and E_1(LO) phonons, which is in agreement with theoretical calculations.[36,40] The broad peak at about 330 cm^{-1} seen in both spectra in Figure 15 is attributed to the second-order Raman processes.

The E_2(high) peak in the spectrum of ZnO QDs is red shifted by 3 cm^{-1} from its position in the bulk ZnO spectrum (see Fig. 15). Since the diameter of the examined ZnO QDs is relatively large, such pronounced red shift of the E_2 (high) phonon peak can hardly be attributed only to the optical phonon confinement by the QD boundaries. Measuring the anti-Stokes spectrum and using the relationship between the temperature T and the relative intensity of Stokes and anti-Stokes peaks $I_S/I_{AS} \approx \exp[\hbar\omega/k_BT]$, we have estimated the temperature of the ZnO QD powder under visible excitation to be below 50°C. Thus, heating in the nonresonant Raman spectra cannot be responsible for the observed frequency shift. Therefore, we conclude that the shift of E_2 (high) phonon mode is due to the presence of intrinsic defects in the ZnO QD samples, which have about 0.5% impurities. This conclusion was supported by a recent study [45] that showed a strong dependence of the E_2 (high) peak on the isotopic composition of ZnO.

Figure 16a and 16b show the measured resonant Raman scattering spectra of bulk ZnO and ZnO QDs, respectively. A number of LO multiphonon peaks are observed in both resonant Raman spectra. The frequency 574 cm^{-1} of 1LO phonon peak in bulk ZnO corresponds to A_1(LO) phonon, which can be observed only in the configuration when the *c*-axis of wurtzite ZnO is parallel to the sample face. When the *c*-axis is perpendicular to the sample face, the E_1(LO) phonon is observed instead. According to the theory of polar optical phonons in wurtzite nanocrystals presented in the previous section, the frequency of 1LO phonon mode in ZnO QDs should be between 574 and 591 cm^{-1}. However, Figure 16b shows that this frequency is only 570 cm^{-1}. The observed red shift of the 1LO peak in the powder of ZnO QDs is too large to be caused by intrinsic defects or

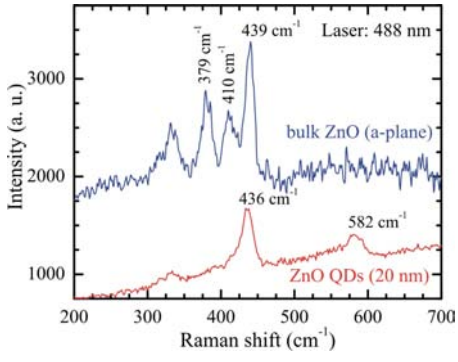

Fig. 15. Nonresonant Raman scattering spectra of bulk ZnO (*a*-plane) and ZnO QDs (20-nm diameter). Laser power is 15 mW. Linear background is subtracted for the bulk ZnO spectrum.

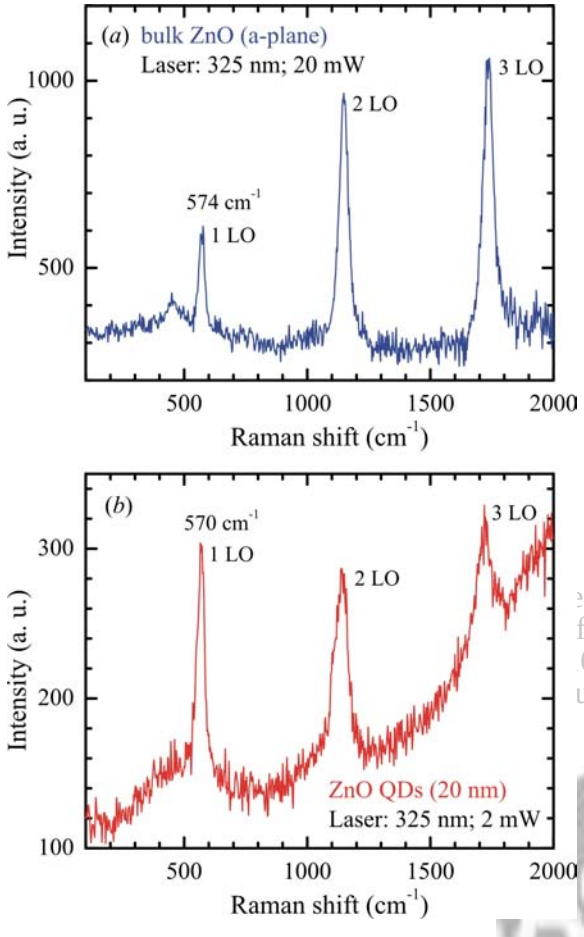

Fig. 16. Resonant Raman scattering spectra of (a) *a*-plane bulk ZnO and (b) ZnO QDs. Laser power is 20 mW for bulk ZnO and 2 mW for ZnO QDs. PL background is subtracted from the bulk ZnO spectrum. Reprinted with permission from Ref. 44, K. A. Alim, V. A. Fonoberov, and A. A. Balandin. *Appl. Phys. Lett.*, 86, 053103 (**2005**). © 2005, American Institute of Physics.

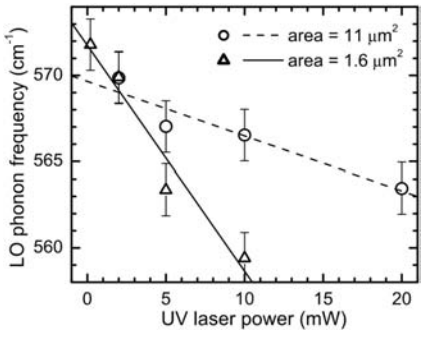

Fig. 17. LO phonon frequency shift in ZnO QDs as a function of the excitation laser power. Laser wavelength is 325 nm. Circles and triangles correspond to the illuminated sample areas of 11 and 1.6 μm^2.

impurities. The only possible explanation for the observed red shift is a local temperature raise induced by UV laser in the powder of ZnO QDs.[46] To check this assumption, we varied the UV laser power as well as the area of the illuminated spot on the ZnO QD powder sample.

Figure 17 shows the LO phonon frequency in the powder of ZnO QDs as a function of UV laser power for two different areas of the illuminated spot. It is seen from Figure 17 that, for the illuminated 11-μm^2 spot, the red shift of the LO peak increases almost linearly with UV laser power and reaches about 7 cm^{-1} for the excitation laser power of 20 mW. As expected, by reducing the area of the illuminated spot to 1.6 μm^2, we get a faster increase of the LO peak red shift with the laser power. In the latter case, the LO peak red shift reaches about 14 cm^{-1} for a laser power of only 10 mW. An attempt to measure the LO phonon frequency using the illuminated spot with an area 1.6 μm^2 and UV laser power 20 mW resulted in the destruction of the ZnO QDs on the illuminated spot, which was confirmed by the absence of any ZnO signature peaks in the measured spectra at any laser power.

It is known that the melting point of ZnO powders is substantially lower than that of a ZnO crystal ($\sim 2000^\circ C$), which results in the ZnO powder evaporation at a temperature less than $1400^\circ C$.[47] The density of the examined ensemble of ZnO QDs is only about 8% of the density of ZnO crystal, which means that there is a large amount of air between the QDs and therefore very small thermal conductivity of the illuminated spot. This explains the origin of such strong excitation laser heating effect on the Raman spectra of ZnO QDs.

If the temperature rise in our sample is proportional to the UV laser power, then the observed 14 cm^{-1} LO phonon red shift should correspond to a temperature rise around $700^\circ C$ at the sample spot of an area 1.6 μm^2 illuminated by the UV laser at a power of 10 mW. In this case, the increase of the laser power to 20 mW would lead to the temperature of about $1400^\circ C$ and the observed destruction of the QD sample spot. To verify this conclusion, we calculated the LO phonon frequency of ZnO as a function of temperature. Taking into account the thermal expansion and anharmonic coupling effects, the LO phonon frequency can be written as[48]

$$\omega(T) = \exp\left[-\gamma \int_0^T \left\{2\alpha_\perp(T') + \alpha_\parallel(T')\right\} dT'\right] \times (\omega_0 - M_1 - M_2) + M_1\left[1 + \frac{2}{e^{\hbar\omega_0/2k_BT} - 1}\right] + M_2\left[1 + \frac{3}{e^{\hbar\omega_0/3k_BT} - 1} + \frac{3}{(e^{\hbar\omega_0/3k_BT} - 1)^2}\right], \quad (34)$$

where the Grüneisen parameter of the LO phonon in ZnO $\gamma = 1.4$,[49] the thermal expansion coefficients $\alpha_\perp(T)$ and $\alpha_\parallel(T)$ for ZnO are taken from Ref. 50, and the anharmonicity parameters M_1 and M_2 are assumed to be equal to those of the A_1(LO) phonon of GaN[48]: $M_1 = -4.14\ cm^{-1}$,

and $M_2 = -0.08\,\mathrm{cm}^{-1}$. By fitting of the experimental data shown in Figure 17 (area = 1.6 $\mu\mathrm{m}^2$) with Eq. (1), the LO phonon frequency at $T = 0\,\mathrm{K}$, ω_0, was found to be $577\,\mathrm{cm}^{-1}$. At the same time, it followed from Eq. (1) that the observed 14-cm^{-1} red shift shown in Figure 17 indeed corresponded to ZnO heated to the temperature of about 700°C.

Thus, we have clarified the origin of the phonon peak shifts in ZnO QDs. By using nonresonant and resonant Raman spectroscopy, we have determined that there are three factors contributing to the observed peak shifts. They are the optical phonon confinement by the QD boundaries, the phonon localization by defects or impurities, and the laser-induced heating in nanostructure ensembles. While the first two factors were found to result in phonon peak shifts of a few cm^{-1}, the third factor, laser-induced heating, could result in the resonant Raman peak red shift as large as tens of cm^{-1}.

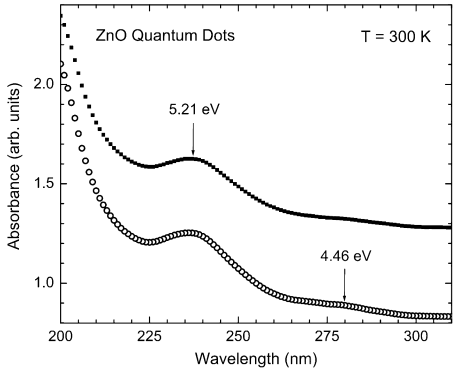

Fig. 18. Optical absorption spectra of ZnO QDs indicating strong quantum confinement. Two curves are taken for the same sample (solution of ZnO QDs) at different times to demonstrate the consistency of the results.

6. PHOTOLUMINESCENCE SPECTROSCOPY OF ZINC OXIDE QUANTUM DOTS

There have been a large number of experimental studies of PL spectra of ZnO QDs. There is noticeable discrepancy in the interpretation of UV emission from ZnO QDs. Part of this discrepancy can be attributed to the differences in ZnO QD synthesis and surface treatment and encapsulation. Another part can be related to the fact that the physics of the carrier recombination in ZnO QDs may indeed be different due to some specifics of the material system, such as low dielectric constant, wurtzite crystal lattice, and large exciton-binding energy. While most of the reports indicated that very low-temperature ($\sim 10\,\mathrm{K}$) UV emission in ZnO is due to the donor-bound excitons, there is no agreement about the mechanism of the emission at higher temperatures. Various investigations arrived at different, and sometimes opposite, conclusions about the origin of UV PL in ZnO nanostructures. For example, UV PL was attributed to the confined excitons[23, 51–55] TO phonon band of the confined excitons,[56, 57] donor-bound excitons,[58, 59] acceptor-bound excitons,[60–62] or donor-acceptor pairs.[63–67]

In this section, we describe some of the features observed in the UV region of PL spectra obtained from ZnO QDs with the average diameter of 4 nm synthesized by the wet chemistry method.[44] The size of the large fraction of the examined QDs is small enough to have quantum confinement of the charge carriers. Figure 18 shows the absorbance spectra of ZnO QDs, which indicate a large blue shift as compared to the bulk band gap of ZnO. In Figure 19, we present PL spectra of the same ZnO QDs as the temperature varies from 8.5 K to 150 K. The spectra were taken under laser excitation with a wavelength of 325 nm. One should keep in mind that the smallest dots, which lead to the large blue shift in the absorbance spectrum, do not contribute to the PL spectra measured under the 325-nm excitation. Assuming the same order of peaks as usually observed for bulk ZnO, we can assign the measured peaks for ZnO QDs (from right to left) to the donor-bound excitons (D, X), acceptor-bound excitons (A, X), and LO phonon peak of the acceptor-bound excitons. The energy of the LO phonon is 72 meV, which is in good agreement with the reported theoretical and experimental data.

An arrow in Figure 19 indicates the location of the confined exciton energy (3.462 eV) calculated by us for ZnO QDs with a diameter of 4.4 nm. Note that, at a given laser excitation, the larger size QDs from the ensemble of 4 ± 0.8 nm are excited; therefore, we attribute the observed PL spectrum to 4.4-nm QDs. No confined exciton peak is seen at 3.462 eV for the considered temperatures, which might be explained by the presence of the surface acceptor impurities in ZnO QDs. The last is not surprising

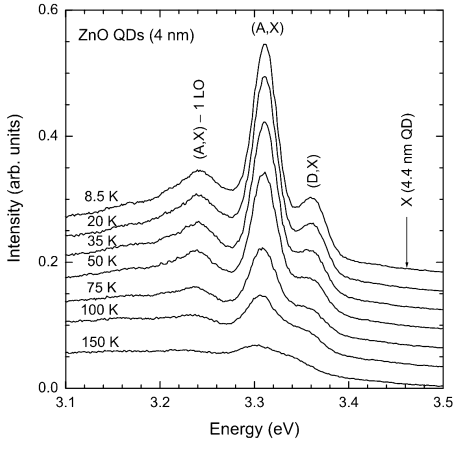

Fig. 19. PL spectra of ZnO QDs for the temperatures from 8.5 K to 150 K. The location of the confined exciton peak is marked with an arrow. The spectra are shifted in the vertical direction for clarity.

given a large surface-to-volume ratio in QDs. It can be estimated from the ZnO lattice constants ($a = 0.3249$ nm, $c = 0.5207$ nm) that one atom occupies a volume of a cube with edge $a_0 = 0.228$ nm. Therefore, one can estimate that the number of surface atoms in the 4.4-nm ZnO QD is about 28% of the total number of atoms in the considered QDs.

Figures 20 and 21 present PL peak energies and PL peak intensities of the donor-bound and acceptor-bound excitons, respectively. The data in Figure 20 suggest that the temperature dependence of the energy of the impurity-bound excitons can be described by the Varshni law, similar to the case of bulk ZnO.[68] The donor-bound exciton energy in the 4-nm ZnO QDs is increased by about 5 meV compared to the bulk value due to quantum confinement of the donor-bound excitons. At the same time, a comparison of the acceptor-bound exciton energies in 4-nm ZnO QDs and in bulk ZnO shows a decrease of about 10 meV for ZnO QDs at temperatures up to 70 K. The observed decrease of the energy of the acceptor-bound excitons in ZnO QDs cannot be explained by confinement. One possible explanation could be the lowering of the impurity potential near the QD surface. Another possibility is that at low temperatures this peak is affected by some additional binding, similar to that in a charged donor-acceptor pair.[65–67] The energy of a donor-acceptor pair in bulk ZnO can be calculated as[65]

$$E_{DAP} = E_g - E_D^{\text{bind}} - E_A^{\text{bind}} + \frac{e^2}{4\pi\,\varepsilon_0 \varepsilon R_{DA}} \qquad (35)$$

where E_g is the band gap (3.437 eV at 2 K), E_D^{bind} is the binding energy of a donor (with respect to the bottom of the conduction band), E_A^{bind} is the binding energy of an acceptor (with respect to the top of valence band), ε_0 is the permittivity of free space, e is the electron charge, $\varepsilon = 8.1$ is the static dielectric constant (inverse average of $\varepsilon_\perp = 7.8$ and $\varepsilon_\parallel = 8.75$), and R_{DA} is the donor-acceptor pair separation. Both electrons and holes are confined inside the ZnO QDs. Therefore, to apply Eq. (35) to ZnO QDs, one has to take into account the confinement-induced increase of E_g, E_D^{bind}, and E_A^{bind}. Since E_g and $E_D^{\text{bind}} + E_A^{\text{bind}}$ enter Eq. (35) with the opposite signs, the effect of confinement is partially cancelled, and in the first approximation, one can employ Eq. (35) for ZnO QDs. Note that E_D^{bind} is about 60 meV for ZnO [65]. The large percentage of surface atoms in the 4.4-nm ZnO QD (28%) allows one to assume that the majority of the acceptors are located at the surface, which is also in agreement with the theoretical results reported by Fonoberov and Balandin.[30]

Due to the relatively small number of atoms (3748) in the 4.4-nm ZnO QD, it is reasonable to assume that there are only 1–2 donor-acceptor pairs in such QDs. Indeed, a typical 10^{19} cm^{-3} concentration of acceptors [65,66] means only 0.5 acceptors per volume of our 4.4-nm QD. Thus, the donor-acceptor pair separation R_{DA} is equal to the average distance from the surface acceptor to the randomly located donor. This average distance is exactly equal to the radius of the considered QD. For the observed donor-acceptor pair, one can find from Eq. (35) 3311 meV = 3437 meV − 60 meV − E_A^{bind} + 80.8 meV. Therefore, the lower limit of the acceptor-binding energy is estimated to be $E_A^{\text{bind}} =$ 146.8 meV, which is in agreement with the reported values 107–212 meV.[64,67] Note that for bulk ZnO, the donor-acceptor peak has been observed at 3.216 eV.[69]

Thus, further study is necessary to determine the origin of the highest peak in Figure 19 for $T < 70$ K. While the origin of low-temperature PL from ZnO QDs can be the same as for higher temperatures (recombination of acceptor-bound excitons), the estimation presented suggests that recombination of donor-acceptor pairs can also be responsible for the observed peak.

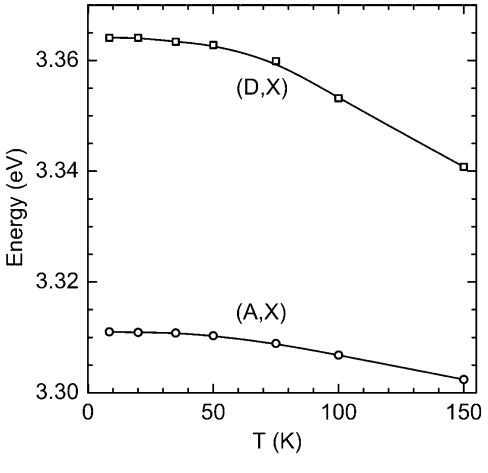

Fig. 20. Peak energies for the donor- and acceptor-bound excitons as a function of temperature in ZnO QDs.

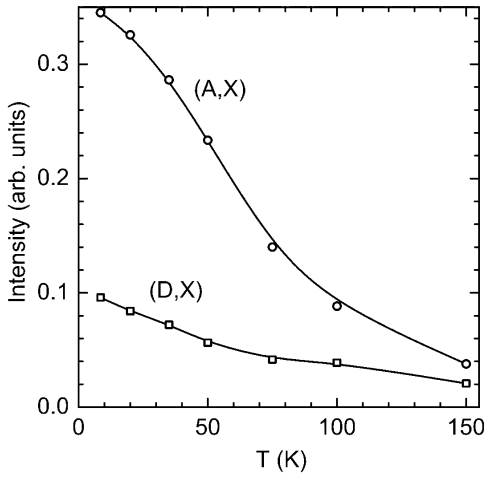

Fig. 21. Intensities of the donor-bound and acceptor-bound exciton peaks as the function of temperature in ZnO QDs.

7. CONCLUSIONS

This review describes exciton states in ZnO QDs in the intermediate quantum confinement regime. The presented theoretical results can be used for interpretation of experimental data. The small radiative lifetime and rather thick "dead layer" in ZnO QDs are expected to be beneficial for optoelectronic device applications. We described in detail the origin of UV PL in ZnO QDs, discussing recombination of confined excitons or surface-bound acceptor–exciton complexes. The review also outlines the analytical approach to interface and confined polar optical phonon modes in spheroidal QDs with wurtzite crystal structure. The presented theory has been applied to investigation of phonon frequencies and potentials in spheroidal freestanding ZnO QDs and those embedded into the MgZnO crystal. A discrete spectrum of frequencies has been obtained for the *interface* polar optical phonons in wurtzite spheroidal QDs. It has been demonstrated that *confined* polar optical phonons in wurtzite QDs have discrete spectrum, while the confined polar optical phonons in zinc blende QDs have a single frequency (LO). The positions of the polar optical phonons in the measured resonant Raman spectra of ZnO QDs were explained quantitatively using the developed theoretical approach. The model described in this review allows one to explain and accurately predict phonon peaks in the Raman spectra not only for wurtzite ZnO nanocrystals, nanorods, and epitaxial ZnO/$Mg_{0.2}Zn_{0.8}O$ QDs, but also for any wurtzite spheroidal QD, either freestanding or embedded into another crystal. In the final section of the review, we outlined PL in ZnO QDs, focusing on the role of acceptor impurities as the centers of exciton recombination. The results described in this review are important for the future development of ZnO technology and optoelectronic applications.

Acknowledgments: The research conducted in the Nano-Device Laboratory (http://ndl.ee.ucr.edu/) has been supported, in part, by the National Science Foundation (NSF), DARPA-SRC MARCO Functional Engineered Nano Architectonic (FENA) Center, and DARPA UCR-UCLA-UCSB Center for Nanoscale Innovations for Defence (CNID). We thank NDL member Khan Alim for providing experimental data on Raman and PL spectroscopy of ZnO QDs.

References

1. S. C. Erwin, L. J. Zu, M. I. Haftel, A. L. Efros, T. A. Kennedy, and D. J. Norris. *Nature*, 436, 91 (**2005**).
2. R. Viswanatha, S. Sapra, B. Satpati, P. V. Satyam, B. N. Dev, and D. D. Sarma. *J. Mater. Chem.*, 14, 661 (**2004**).
3. L. Brus. *J. Phys. Chem.*, 90, 2555 (**1986**).
4. L. E. Brus. *J. Chem. Phys.*, 80, 4403 (**1984**).
5. M. Califano, A. Zunger, and A. Franceschetti. *Nano Lett.*, 4, 525 (**2004**).
6. V. A. Fonoberov, E. P. Pokatilov, V. M. Fomin, and J. T. Devreese. *Phys. Rev. Lett.*, 92, 127402 (**2004**).
7. A. Mews, A. V. Kadavanich, U. Banin, and A. P. Alivisatos. *Phys. Rev. B*, 53, R13242 (**1996**).
8. V. A. Fonoberov and A. A. Balandin. *Phys. Rev. B*, 70, 195410 (**2004**).
9. W. R. L. Lambrecht, A. V. Rodina, S. Limpijumnong, B. Segall, and B. K. Meyer. *Phys. Rev. B*, 65, 075207 (**2002**).
10. D. C. Reynolds, D. C. Look, B. Jogai, C. W. Litton, G. Cantwell, and W. C. Harsch. *Phys. Rev. B*, 60, 2340 (**1999**).
11. A. Kobayashi, O. F. Sankey, S. M. Volz, and J. D. Dow. *Phys. Rev. B*, 28, 935 (**1983**).
12. Y. Kayanuma. *Phys. Rev. B*, 38, 9797 (**1988**).
13. V. A. Fonoberov and A. A. Balandin. *J. Appl. Phys.* 94, 7178 (**2003**).
14. V. A. Fonoberov, E. P. Pokatilov, and A. A. Balandin. *Phys. Rev. B*, 66, 085310 (**2002**).
15. E. A. Muelenkamp. *J. Phys. Chem. B*, 102, 5566 (**1998**).
16. A. Wood, M. Giersig, M. Hilgendorff, A. Vilas-Campos, L. M. Liz-Marzan, and P. Mulvaney. *Aust. J. Chem.*, 56, 1051 (**2003**).
17. P. Lawaetz. *Phys. Rev. B*, 4, 3460 (**1971**).
18. S. I. Pekar, *Sov. Phys. JETP*, 6, 785 (**1958**).
19. M. Combescot, R. Combescot, and B. Roulet. *Eur. Phys. J., B23*, 139 (**2001**).
20. D. C. Reynolds, D. C. Look, B. Jogai, J. E. Hoelscher, R. E. Sherriff, M. T. Harris, and M. J. Callahan. *J. Appl. Phys.*, 88, 2152 (**2000**).
21. E. I. Rashba and G. E. Gurgenishvili. *Sov. Phys. Solid State*, 4, 759 (**1962**).
22. D. W. Bahnemann, C. Kormann, and M. R. Hoffmann. *J. Phys. Chem.*, 91, 3789 (**1987**).
23. E. M. Wong and P. C. Searson. *Appl. Phys. Lett.*, 74, 2939 (**1999**).
24. H. Zhou, H. Alves, D. M. Hofmann, W. Kriegseis, B. K. Meyer, G. Kaczmarczyk, and A. Hoffmann. *Appl. Phys. Lett.*, 80, 210 (**2002**).
25. A. Dijken, E. A. Muelenkamp, D. Vanmaekelbergh, and A. Meijerink. *J. Phys. Chem. B*, 104, 1715 (**2000**).
26. L. Guo, S. Yang, C. Yang, P. Yu, J. Wang, W. Ge, and G. K. L. Wong. *Appl. Phys. Lett.*, 76, 2901 (**2000**).
27. S. Mahamuni, K. Borgohain, B. S. Bendre, V. J. Leppert, and S. H. Risbud. *J. Appl. Phys.*, 85, 2861 (**1999**).
28. L. W. Wang and A. Zunger. *Phys. Rev. B*, 53, 9579 (**1996**).
29. L. W. Wang. *J. Phys. Chem. B*, 105, 2360 (**2001**).
30. V. A. Fonoberov and A. A. Balandin. *Appl. Phys. Lett.*, 85, 5971 (**2004**).
31. R. Englman and R. Ruppin. *Phys. Rev. Lett.*, 16, 898 (**1966**).
32. P. A. Knipp and T. L. Reinecke. *Phys. Rev. B*, 46, 10310 (**1992**).
33. F. Comas, G. Trallero-Giner, N. Studart, and G. E. Marques. *J. Phys.: Condens. Matter,* 14, 6469 (**2002**).
34. S. N. Klimin, E. P. Pokatilov, and V. M. Fomin. *Phys. Stat. Sol. B*, 184, 373 (**1994**).
35. E. P. Pokatilov, S. N. Klimin, V. M. Fomin, J. T. Devreese, and F. W. Wise. *Phys. Rev. B*, 65, 075316 (**2002**).
36. V. A. Fonoberov and A. A. Balandin. *Phys. Rev. B*, 70, 233205 (**2004**).
37. M. A. Stroscio and M. Dutta, Phonons in Nanostructures, Cambridge University Press, Cambridge, U.K. (**2001**).
38. C. Chen, M. Dutta, and M. A. Stroscio. *Phys. Rev. B*, 70, 075316 (**2004**).
39. C. A. Arguello, D. L. Rousseau, and S. P. S. Porto. *Phys. Rev.*, 181, 1351 (**1969**).
40. V. A. Fonoberov and A. A. Balandin. *J. Phys.: Condens. Matter* 17, 1085 (**2005**).
41. C. Bundesmann, M. Schubert, D. Spemann, T. Butz, M. Lorenz, E. M. Kaidashev, M. Grundmann, N. Ashkenov, H. Neumann, and G. Wagner. *Appl. Phys. Lett.*, 81, 2376 (**2002**).
42. M. Rajalakshmi, A. K. Arora, B. S. Bendre, and S. Mahamuni. *J. Appl. Phys.* 87, 2445 (**2000**).
43. H. Richter, Z. P. Wang, and L. Ley. *Solid State Commun.* 39, 625 (**1981**).
44. K. A. Alim, V. A. Fonoberov, and A. A. Balandin. *Appl. Phys. Lett.*, 86, 053103 (**2005**).
45. J. Serrano, F. J. Manjon, A. H. Romero, F. Widulle, R. Lauck, and M. Cardona. *Phys. Rev. Lett.*, 90, 055510 (**2003**).
46. L. Bergman, X. B. Chen, J. L. Morrison, J. Huso, and A. P. Purdy. *J. Appl. Phys.*, 96, 675 (**2004**).
47. K. Park, J. S. Lee, M. Y. Sung, and S. Kim, *Jpn. J. Appl. Phys.*, 41, 7317 (**2002**).

48. W. S. Li, Z. X. Shen, Z. C. Feng, and S. J. Chua. *J. Appl. Phys.*, 87, 3332 (**2000**).
49. F. Decremps, J. Pellicer-Porres, A. M. Saitta, J. C. Chervin, and A. Polian. *Phys. Rev. B*, 65, 092101 (**2002**).
50. H. Iwanaga, A. Kunishige, and S. Takeuchi. *J. Mater. Sci.*, 35, 2451 (**2000**).
51. S. Mahamuni, K. Borgohain, B. S. Bendre, V. J. Leppert, and S. H. Risbud. *J. Appl. Phys.*, 85, 2861 (**1999**).
52. Y. L. Liu, Y. C. Liu, W. Feng, J. Y. Zhang, Y. M. Lu, D. Z. Shen, X. W. Fan, D. J. Wang, and Q. D. Zhao. *J. Chem. Phys.*, 122, 174703 (**2005**).
53. D. M. Bagnall, Y. F. Chen, Z. Zhu, and T. Yao, M. Y. Shen, and T. Goto. *Appl. Phys. Lett.*, 73, 1038 (**1998**).
54. H. J. Ko, Y. F. Chen, Z. Zhu, T. Yao, I. Kobayashi, and H. Uchiki. *Appl. Phys. Lett.*, 76, 1905 (**2000**).
55. D. G. Kim, T. Terashita, I. Tanaka, and M. Nakayama. *Jpn. J. Appl. Phys.* 42, L935 (**2003**).
56. T. Matsumoto, H. Kato, K. Miyamoto, M. Sano, and E. A. Zhukov. *Appl. Phys. Lett.*, 81, 1231 (**2002**).
57. Y. Zhang, B. Lin, X. Sun, and Z. Fu. *Appl. Phys. Lett.*, 86, 131910 (**2005**).
58. H. Najafov, Y. Fukada, S. Ohshio, S. Iida, and H. Saitoh. *Jpn. J. Appl. Phys.*, 42 3490 (**2003**).
59. T. Fujita, J. Chen, and D. Kawaguchi. *Jpn. J. Appl. Phys.*, 42, L834 (**2003**).
60. X. T. Zhang, Y. C. Liu, Z. Z. Zhi, J. Y. Zhang, Y. M. Lu, D. Z. Shen, W. Xu, X. W. Fan, and X. G. Kong. J. Lumin., 99, 149 (**2002**).
61. J. Chen and T. Fujita. *Jpn. J. Appl. Phys.*, 41, L203 (**2002**).
62. C. R. Gorla, N. W. Emanetoglu, S. Liang, W. E. Mayo, Y. Lu, M. Wraback, and H. Shen. *J. Appl. Phys.*, 85, 2595 (**1999**).
63. S. Ozaki, T. Tsuchiya, Y. Inokuchi, and S. Adachi. *Phys. Status Solidi A*, 202, 1325 (**2005**).
64. B. P. Zhang, N. T. Binh, Y. Segawa, K. Wakatsuki, and N. Usami. *Appl. Phys. Lett.*, 83, 1635 (**2003**).
65. D. C. Look, D. C. Reynolds, C. W. Litton, R. L. Jones, D. B. Eason, and G. Cantwell. *Appl. Phys. Lett.*, 81, 1830 (**2002**).
66. H. W. Liang, Y. M. Lu, D. Z. Shen, Y. C. Liu, J. F. Yan, C. X. Shan, B. H. Li, Z. Z. Zhang, J. Y. Zhang, and X. W. Fan. *Phys. Status Solidi A*, 202, 1060 (**2005**).
67. F. X. Xiu, Z. Yang, L. J. Mandalapu, D. T. Zhao, J. L. Liu, and W. P. Beyermann. *Appl. Phys. Lett.*, 87, 152101 (**2005**).
68. Y. P. Varshni. *Physica* (Amsterdam), 34, 149 (**1967**).
69. K. Thonke, T. Gruber, N. Teofilov, R. Schönfelder, A. Waag, and R. Sauer. *Physica B*, 308–310, 945 (**2001**).